Rock Mechanics and Rock Engineering
https://doi.org/10.1007/s00603-024-04024-z

ORIGINAL PAPER

Damage-Seepage Evolution Mechanism of Fractured Rock Masses Considering the Influence of Lateral Stress on Fracture Deformation Under Loading and Unloading Process

Xinrong Liu[1,2] · **Jilu Zhang**[1,2] · **Xiaohan Zhou**[1,2] · **Yuyu Liu**[1,2] · **Yan Wang**[1,2] · **Xinyang Luo**[1,2]

Received: 12 January 2024 / Accepted: 6 June 2024

Abstract

Fractures serve as the main pathways for the occurrence and transportation of gases within rock layers. Studying the seepage characteristics of fractured rock masses during loading and unloading processes is an essential issue for understanding the mechanism of hazardous gas migration in surrounding rock under tunnel excavation action. Experiments on rock mass seepage under different precast fracture angles and confining pressures during the loading and unloading process were conducted by using a multi-field coupled triaxial testing system. The findings of the tests indicate that the lateral stress, particularly during the unloading stage, induces the volumetric expansion of fracture. However, the influence of the fracture angle on rock mass fracture expansion is greater than that of the confining pressure. Moreover, the effect of the lateral stress on the fracture surface increases the permeability of the rock mass, nevertheless, the permeability decreases with increasing the confining pressure and decreasing the fracture angle. Under the same stress level value, during the loading stage, the permeability of the rock mass linearly decreases with increasing the confining pressure, while during the unloading stage, the permeability of the rock mass decreases nonlinearly with increasing the confining pressure. Based on the test results, a fluid–solid-damage coupling computational model for the fractured rock mass's permeability was established by considering the influence of the lateral stress on the fracture surface. In addition, further analysis related to the evolution process of the damage and the rock mass seepage has been done. The result reveals that the change in χ with increasing confining pressure exhibits logarithmic characteristics. As the fracture angle decreases, the respective variation ranges of χ are: 0.005~0.03, 016~0.17, 0.2~0.22.

Highlights

- The lateral stress causes volumetric expansion of fracture.
- The effect of lateral stress on fracture surface increases the permeability of rock mass.
- Proposed a calculation model for permeability of fractured rock considering the influence of lateral stress on the fracture surface.
- The change in χ with increasing confining pressure exhibits logarithmic characteristics.

Keywords Fractured rock mass · Fracture angle · Seepage · Lateral stress · Damage

✉ Xiaohan Zhou
cqzhouxhan@126.com

[1] School of Civil Engineering, Chongqing University, Chongqing 400045, China

[2] National Joint Engineering Research Center of Geohazards Prevention in The Reservoir Areas (Chongqing), Chongqing 400045, China

Published online: 27 August 2024

List of Symbols

ε_1	Major principal strains
ε_3	Minor principal strains
ε_v	Volumetric strain
ε_{ev}	Elastic strain of the rock matrix
ε_{fv}	Fracture volumetric strain
μ	Poisson's ratio
E	Elastic modulus, GPa
d_f	Equivalent hydraulic aperture, m
υ	Kinematic viscosity of the fluid, m^2/s
L	Length of the fracture, m
Q	Fluid flow rate, m^3/s
ω	Width of the fracture, m
Δp	Pressure difference between the inlet and outlet, Pa
K_f	Permeability of rock mass, m^2
Re	Reynolds number
ρ_g	Fluid density, kg/m^3
μ_g	Dynamic viscosity of the fluid, Pa·s
G	Shear modulus of the rock mass, GPa
α	Biot's coefficient
Φ	Rock mass porosity
Φ_0	Initial rock mass porosity
Φ_r	Rock mass porosity after failure
t	Time, s
Q_m	Source term, $kg/(m^3 \cdot s)$
F_1, F_2	State functions of tension and shear stress
f_{t0}	Uniaxial tensile strength, MPa
f_{c0}	Uniaxial compressive strength, MPa
φ	Internal friction angle of the rock mass, deg
n	Damage evolution coefficient
θ	Precast fracture angle, deg
ε_{t0}	Maximum principal strains corresponding to tensile damage
ε_{c0}	Maximum principal strains corresponding to shear damage
E_0	Initial elastic modulus, GPa
α_k	Stress sensitivity coefficient of the porosity
σ_n	Normal stress of the fracture surface, MPa
k_n	Normal stiffness, N/m^2
χ	Lateral stress influence coefficient on normal deformation

1 Introduction

With the development of deep underground spaces, incidents of hazardous gas outbursts in surrounding rock are increasing (Zhang et al. 2019; Ding and Yue 2022; Yang et al. 2018; Liu et al. 2018a). Fractures serve as the primary pathways for fluid seepage within rock masses. Investigating the effect of the fluid–solid coupling characteristics of fractured rock masses is a prerequisite for ensuring engineering safety in gas-rich areas. The excavation process of underground spaces, coupled with the loading and unloading of the surrounding rocks, leads to changes in the stress state, causing the expansion of fractures within the rock mass. This alteration, especially during rock failure, significantly affects the flow state of fluids within the surrounding rock, and the formation of a rupture plane plays a crucial role in permeability changes (Gong et al. 2022; Ma et al. 2022; Watanabe et al. 2008; Gu et al. 2023; Yan et al. 2022). Therefore, studying the evolution characteristics of fluid flow in fractured rock masses under loading and unloading conditions is of significant importance for predicting and preventing hazardous gas outbursts in regions with complex geological structures.

The fractures of natural rock masses exhibit complex geometric structures. To facilitate the expression of the mechanics and permeability of fractured rock masses, these fractures are often simplified. Many scholars have conducted research on the fluid–solid coupling characteristics in fractured rock masses under the influence of different geometric structures. Wang and Xie (2022) studied the failure modes of rock masses with multiple non-parallel fractures under the influence of fluid–solid coupling. Additionally, based on the inclusion theory, the formula for calculating the increased water pressure resulting from the alteration in the external stress state of fracture water within the rock mass was obtained. Zhang et al. (2022a) performed uniaxial compression experiments on rock masses to investigate the impact of geometric characteristics of fractures (such as length, penetration, quantity, and dip angle) on rock strength. The study explored the evolutionary laws of fracture propagation from both macroscopic and microscopic perspectives. Song et al. (2023) investigated the influence of joint bedding angles and confining pressure on rock strength and energy dissipation by H-M coupling triaxial loading and unloading tests. Based on the domino effect and structural evolution theory, the study revealed the way of energy dissipation and the fracture mechanisms of layered sandstone under hydraulic-mechanical coupling conditions. Zhang et al. (2022b) employed a 3D bonded block model (BBM) to quantitatively analyze the strength and permeability of fractured rock masses. The results of the investigation showed a positive correlation between fracture stiffness, the friction angle and the strength of fractured rock masses. Additionally, the permeability is positively related to the strength for rock masses that are impermeable in the pre-peak loading phase.

The deformation and damage behavior of rock masses under different stress conditions affect the aperture and expansion of fractures, therefore affecting the rock mass's permeability (Singh 1997; Vu et al. 2017; Walsh et al. 2008; Katsuki et al. 2019). Currently, research on the damage and permeability characteristics of fractured rock masses under triaxial stress conditions is mostly conducted by using non-through-going fractures. Du et al. (2020) investigated the evolution law of rock permeability under the effect of crack propagation employing sandstone samples with two preexisting fissures. The study reveals that the impact of ligament length and bridge angle on the permeability shows an inverse relationship with confining pressure nevertheless a direct relationship with the water pressure has appeared. Furthermore, the permeability sequence during various stages of rock crack propagation is as follows: $k_{cd} < k_{ci} < k_c < k_0 < k_{\max}$; In order to determine the stress intensity factor at the crack tip under permeation creep conditions, Zhang et al. (2024) performed creep tests on artificially filled single fracture sandstone specimens under multi-level seepage pressure. They also proposed a strength criterion and a critical seepage pressure for crack initiation under the coupling effect of creep and permeation. Additionally, it was discovered that the fissure inclination angle is the second most important governing element affecting the permeation characteristics of cracked sandstone, after the filling condition. Yang and Hu (2020) studied the evolution characteristics of creep and permeation in red sandstone specimens with single fissures under cyclic loading conditions. The results show that stress and deformation have an impact on the permeability of fissured sandstone, which varies over time and decreases with increasing load and increases with decreasing unloading. Additionally, in multiple loading and unloading cycles, upon the third occurrence of creep, the permeability initially decreases before suddenly rising. However, in low-porosity rock formations, gases are often trapped within fractures of rock. Due to the dense distribution of fractures, fractures within such areas are considered to be in a connected state. Therefore, rather than affecting the growth and development of non-through-going fractures, changes in stress conditions primarily affect the permeability of fractures by modifying their aperture. Even, the research findings on the expansion and permeation evolution of non-through-going fractures may not fully apply to connected fractures. For the above reasons, the researchers have conducted extensive work on the permeation characteristics of through-going fractured rock masses. Wang et al. (2021) proposed a new permeability calculation model combining the deformation of crack closure based on hydraulic aperture with the Goodman hyperbolic model to study the influence of confining pressure (Pc) on the characteristics of the seepage mechanism. The model was validated by fluid mechanics experiments under different confining pressures on single fractured rock samples. The results showed that the higher the flow rate, the higher the accuracy of the model calculations. To explore the seepage behavior of interconnected fractures, Ma et al. (2023a) established an experimental system based on the fluid–solid coupling method. Experiments revealed that fluid showing flexural flow behavior is caused by the closure effects of load and contact area on bifurcation fracture surfaces. The side of the bifurcated crack with the bigger bifurcation angle suffers stronger closure effects at different degrees of confining pressure, which in turn promotes the flexural flow of fluid in the fracture on the other side. Ma et al. (2013) conducted hydraulic coupling tests on fractured mudstone, limestone, and sandstone samples under different confining pressures to investigate the relationship between permeability characteristics and confining pressure. The study revealed that the permeability of fractured rock masses exhibits a trend of rapid exponential decline initially, followed by a slower power-law decline as the confining pressure increases. Additionally, sandstone exhibits higher permeability compared to mudstone and limestone. Existing studies mostly focus on the permeation characteristics of through-going fractured rock masses under the influence of confining pressure. However, actual geological formations are often subjected to triaxial non-uniform stress states. The impact of lateral stress on the fracture surface on the features of rock mass permeation has not received much attention in the literature, particularly in the context of deep underground engineering construction where unloading may result in larger triaxial non-uniform stress states. It is yet unknown how rock mass permeation evolves when lateral stress and damage act together.

In this study, loading–unloading tests were conducted on rock masses with the influence of precast fracture angles and confining pressures. The research analyzed the deformation behavior and the seepage characteristics of the rock mass. Moreover, the failure mechanism of rock mass has been revealed. Based on the elastic damage theory, the seepage theory of porous and fracture media and the effective stress principle, a computational model for the coupling of fluid–solid-damage in fractured rock masses was established considering the influence of lateral stress on the fracture deformation. The model was applied through secondary development of numerical simulations and further explored the characteristic of seepage in fractured rock masses during the entire process of loading and unloading. Furthermore, analyzing the damage evolution characteristics of rock masses under different stress conditions has been accomplished.

2 Test Overview

2.1 Sample Preparation

The selected rock for the experiment is from the surrounding rock of a tunnel located in Linzhi city, China. The tunnel traverses a fault zone, which reveals the presence of CO_2 gas in the surrounding rock. The rock has an average density of 2621.4 kg/m^3, uniaxial compressive strength of 144 MPa, and uniaxial tensile strength of 6 MPa. According to XRD diffraction analysis, the mineral composition

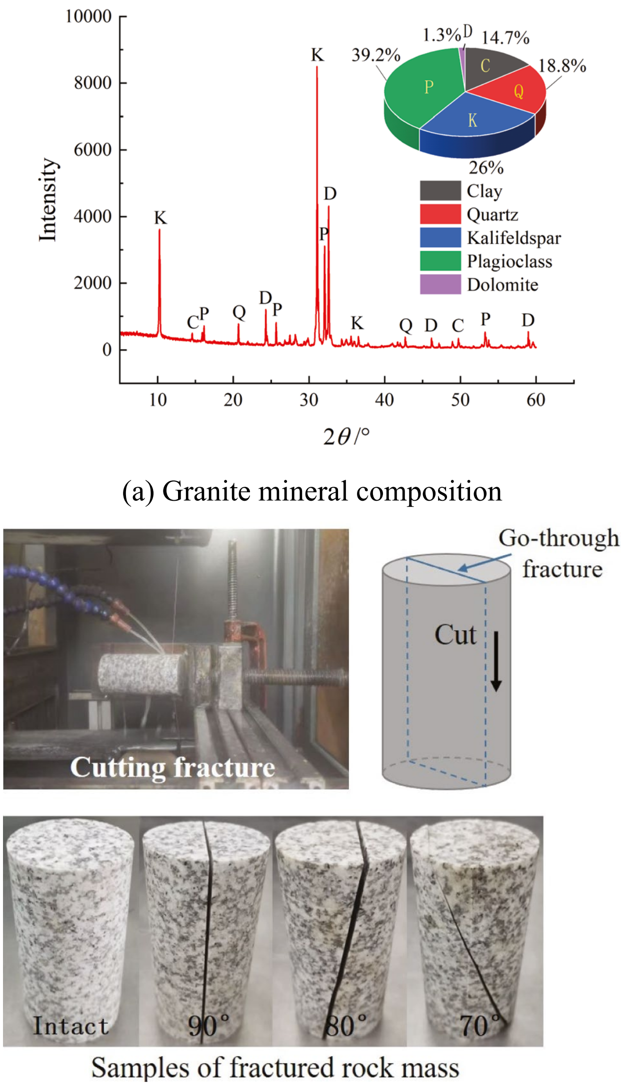

(a) Granite mineral composition

(b) Preparation of penetrating fractured rock mass

Fig. 1 Rock preparation and testing

of the in-situ surrounding rock is mainly composed of plagioclase (39.2%), kalifeldspar (26%), quartz (18.8%), clay (14.7%) and dolomite (1.3%) (Fig. 1a). According to relevant testing standards (Li and Liu 2021), intact and uniformly mineral-distributed rocks were selected and prepared as standard samples with dimensions of φ50 mm × H100 mm. Subsequently, different angle of precast penetrating fractured rock masses was created. The orientation between the natural fractures within the rock strata and the principal stress is not perpendicular. Due to the stochastic development of fractures, it is impossible to determine the relationship between the principal stress and fracture angles on a small scale.

However, the orientation and inclination of the fault zones are in line with the macrostructures of rock mass fractures in the fault zone-affected region. Thus, the study focuses on the relationship between the inclination of fault zones and the principal stress. On-site tunneling traverses fault zones with angles ranging from 70° to 90°. The angles of 70°, 80°, and 90° were chosen for penetrating fractured angles. To facilitate the expression of the mechanical and permeation laws of fractured rock masses, the fractures are simplified and presented as through-going fractured rock masses with different angles. To ensure that the different degrees of closure of through-going fractures do not affect the test results, sand line cutting is used for the specimens, with a cutting precision of ±0.03 mm. The fracture surfaces can be approximately considered as smooth planes, and the fractures can be regarded as adequately closed during the test process, the specific is shown in Fig. 1b.

2.2 Experimental Design and Procedures

The schematic diagram in Fig. 2 illustrates the variation of stress and gas seepage in the surrounding rock during the excavation of a tunnel in a fault zone. As the axial stress loads, the rock mass in front of the tunnel face experiences the unloading of confining stress. Therefore, during applying the axial stress loading, the stress path in the unloading process of the triaxial test follows the unloading of confining stress. On-site, the maximum principal stress in the tunnel construction area obtained via borehole release method (Sazid et al. 2023; Mukai et al. 2007; Al-Bakri and Sazid 2023) is approximately 40 MPa, with the major principal stress aligned with the direction of gravity, and the lateral stress coefficient is about 0.9, indicating that the confining pressure in experiments is within 36 MPa. In existing research, the unloading starting point for triaxial tests often falls between 70 to 80% of the triaxial compressive strength. This study adopts an unloading start point of 70% of the triaxial compressive strength (Liu et al. 2018b). Additionally, the storage pressure of CO_2 in the strata is generally within 3 MPa (Yuan et al. 2022; Huo et al. 2021). Thus, 3 MPa is chosen as the gas seepage pressure in this experiment. Tables 1 and 2 represent the peak stress under triaxial loading for the rock mass and the conditions of the triaxial loading and unloading tests on the rock mass, respectively. The variation of intact rock mechanical parameters with confining pressure is illustrated in Fig. 3.

According to the relevant experimental testing guidelines and procedures (Zhang et al. 2021), the following steps are the procedures for the seepage test by using rock mass loading and unloading:

(1) After inserting the rock mass sample into the triaxial pressure chamber, the circumferential and vertical strain sensors have been installed.
(2) The confining pressure will be applied through using the stress control method, in this method the confining

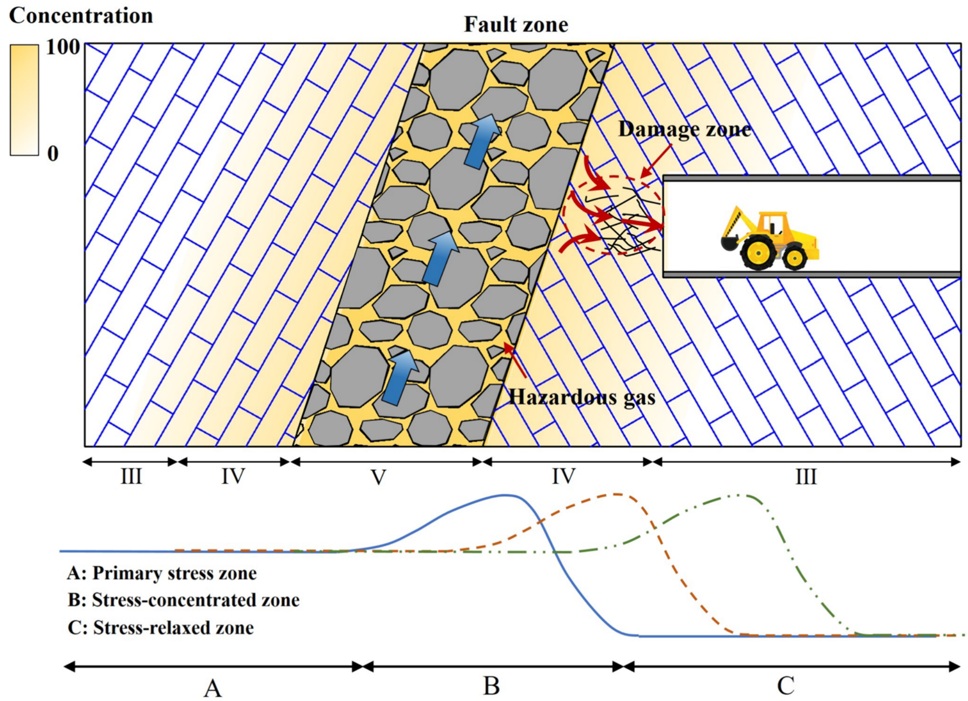

Fig. 2 Schematic of the variation of stress and gas seepage in the surrounding rock during the excavation of a tunnel in a fault zone

Table 1 Peak stress under triaxial loading for rock mass

Number	Confining pressure σ_3/MPa	Precast fracture angle θ/°	Peak stress σ_c/MPa
A-1	15	No fracture	275.1
A-2	25	No fracture	355.2
A-3	35	No fracture	418.2
A-4	15	90	250.1
A-5	25	90	339.4
A-6	35	90	396.3
A-7	15	80	236.6
A-8	25	80	290.0
A-9	35	80	343.3
A-10	15	70	95.7
A-11	25	70	131.1
A-12	35	70	163.2

Table 2 Triaxial loading and unloading conditions for penetrating fractured rock mass

Number	Confining pressure σ_3/MPa	Precast fracture angle θ/°	Seepage pressure P/MPa	Unloading strating stress σ_u/MPa
U-1	15	90	3	175.1
U-2	25	90	3	237.6
U-3	35	90	3	277.4
U-4	15	80	3	165.6
U-5	25	80	3	203.0
U-6	35	80	3	240.3
U-7	15	70	3	67.0
U-8	25	70	3	91.8
U-9	35	70	3	114.2

pressure will be applied until reaching the design value (P2), with a loading rate of 2 MPa/min.

(3) Open the gas cylinder valve manually, then use the pressure reduction valve to set the CO_2 seepage pressure (P3) equal to the design value. In order to monitor the changes in the flow rate-time curve, open the data monitoring interface. When the flow rate no longer shows significant variations with time, it is considered that the seepage has reached a stable state, for this circumstance, the flow rate at this point is regarded as the beginning of the seepage rate.

(4) Apply axial load (P1) using the displacement control method until reaching the unloading starting stress, with an axial stress loading rate of 0.1 mm/min.

(5) Unload the confining pressure in stress control mode at a rate of 2 MPa/min, while still applying axial displacement at a rate of 0.1 mm/min, until the sample failure.

(6) Stop data collection, unload the gas pressure, axial pressure, and confining pressure sequentially, and finally remove the sample from the pressure chamber.

2.3 Experimental Equipment

The experiment utilized the Rock 600-50 triaxial and multi-field coupling rock mechanical test system (Fig. 4), which

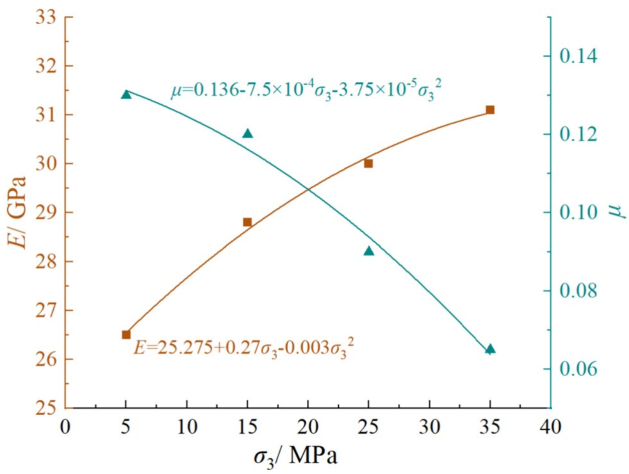

Fig. 3 Variation of intact rock mechanical parameters with confining pressure

allows for multi-field coupling tests under multiphase flow conditions. The equipment can apply a maximum axial pressure of 500 MPa, a confining pressure of 60 MPa, and a maximum seepage pressure of 60 MPa. The triaxial pressure chamber is equipped with LVDT axial sensors (measurement accuracy: ≤0.001 mm; measurement range: ±5 mm) and 360° close-fitting radial deformation sensors (measurement range: ≤3%; measurement accuracy: ≤±0.001 mm). The fluid sensor has an effective measurement range of 0.001 ml/min to 500 ml/min with a measurement accuracy of 0.001 ml. The equipment has a maximum loading speed of ≥5 MPa/min and a minimum loading speed of ≤0.1 MPa/min.

2.4 Research Methods and Principles

2.4.1 Methods of Calculating Fracture Strain in Rock Mass

Rock is a natural heterogeneous material, and the stress concentration is generated within it due to the presence of inherent microfractures, pores, and bonding surfaces between different mineral components. This leads to fracture occurrence and ultimately failure under external loads. The damage-failure process of brittle rocks is closely related to the generation and propagation of internal fractures in the rock. Therefore, during the loading process, it is usually accompanied by different degrees of volumetric strain. The relationship between volumetric strain (ε_v) and principal strains (ε_1 and ε_3) can be expressed by Eq. (1) (Li et al. 2023).

$$\varepsilon_v = \varepsilon_1 + 2\varepsilon_3 \tag{1}$$

For intact rocks, volumetric strain mainly consists of the elastic strain of the rock matrix (ε_{ev}) and the fracture volumetric strain (ε_{fv}). In fractured rock masses, the volumetric strain of crack fractures is composed of both precast fractures and newly generated fractures within the rock. The volumetric strain of the intact rock can be calculated from the elastic modulus and Poisson's ratio of the intact rock, while the strain

Fig. 4 Triaxial and multi-field coupling rock mechanical test system

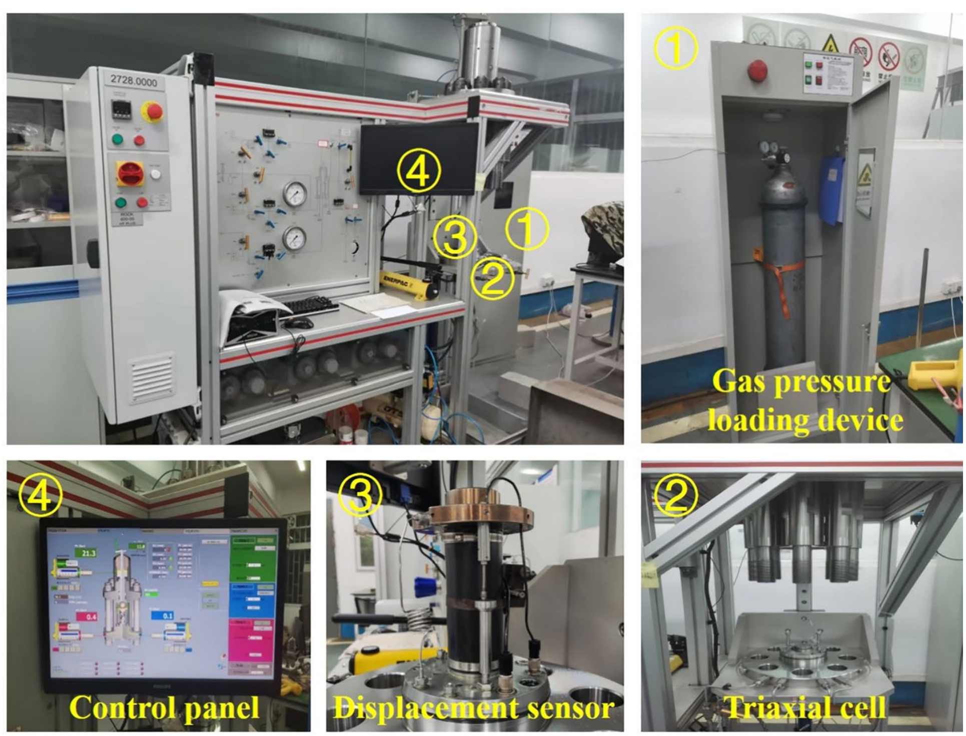

of the rock mass with fractures can be calculated using the methods described in Eqs. (2)~(4).

$$\varepsilon_{\mathrm{v}} = \varepsilon_{\mathrm{ev}} + \varepsilon_{\mathrm{fv}} \tag{2}$$

$$\varepsilon_{\mathrm{ev}} = \frac{1-2\mu}{E}(\sigma_1 + 2\sigma_3) \tag{3}$$

$$\varepsilon_{\mathrm{fv}} = \varepsilon_{\mathrm{v}} - \frac{1-2\mu}{E}(\sigma_1 + 2\sigma_3) \tag{4}$$

2.4.2 Calculation Methods for Fractured Rock Mass Permeability

Existing research indicates that under low-speed conditions, gas flow within fractures follows the cubic law. Due to the typically low porosity of granite in the range of 0.3–0.7%, and the matrix permeability of the rock usually being in the range of 10^{-19} to 10^{-17} m^2 (Wang et al. 2014, 2020), the flow in fractured granite rock mass mainly occurs through the fractures. The permeability of fractured rock mass can be calculated by Eqs. (5)~(6).

$$d_f = \left(\frac{12\upsilon LQ}{\omega g\Delta p}\right)^{1/3} \tag{5}$$

$$K_f = \frac{d_f^2}{12} \tag{6}$$

where d_f is equivalent hydraulic aperture (m), υ is the kinematic viscosity of the fluid (m^2/s), L is the length of the fracture (m), Q is the fluid flow rate (m^3/s), ω is the width of the fracture (m), Δp is the pressure difference between the inlet and outlet (Pa), K_f is the permeability of rock mass (m^2).

3 Experimental Results and Analysis

3.1 Stress–Strain Characteristics of Fractured Rock Mass

The stress–strain curve and volumetric strain-axial strain curve of the fractured rock mass are shown in Fig. 5. The deformation of the rock mass during the loading and unloading process can be divided into five stages: Stage I (OA) is the compaction stage. In this stage, the original fractures in the rock matrix and the precast penetrating fractures will be closed under axial compression. The stress–strain curve shows a concave-up development, and the upper limit stress of this stage being the closure stress of the rock mass fractures, σ_{cc}. Stage II (AB) is the elastic deformation stage. In this stage, the stress–strain curve develops linearly, and the upper limit stress of this stage being the initiation stress of the rock mass, σ_{ci}. Stage III (BC) is the stable propagation stage of fractures. In this stage, the stress–strain curve shows a slight concave down as new microfractures develop within the rock under axial compression. The upper limit stress of this stage is the damage stress of rock mass, σ_{cd}. The rapid propagation stage of fractures is known as stage IV (CD). In this stage, under the effect of the axial compression the stress–strain curve exhibits a pronounced concave down trend as the fractures within the rock rapidly expand. The upper limit of this stage is the peak stress of the rock mass, σ_c. Stage V (DE) is the post-peak failure stage, where the rock mass experiences through-going rupture, corresponding to the residual stress σ_{cr}.

The previous curves show the changes in volumetric strain of rock mass and volumetric strain of fracture. However, the analysis reveals the real behavior of two main issues which are the following: (1) the varying degrees of contraction during the loading phase, (2) the expansion during the unloading phase. Moreover, the extent of volumetric expansion decreases with increasing the confining pressure and increases with the decreasing of precast fracture angle. Furthermore, the analysis of different development stages reveals the following results: in the compaction stage (OA), the closure of the microfractures and precast fractures in the rock leads to a significant volume contraction in both the rock and the fracture with the increase in axial strain. Further volumetric strain contraction in the rock mass body and fracture will be observed in the elastic deformation stage (AB) when axial strain increases. Variations in precast fracture angle and confining pressure have a greater impact on the volumetric strain of the fracture. Overall, the degree of fracture volumetric strain contraction increases with increasing the confining pressure. Nevertheless, it decreases with the increase in precast fracture angle. When the precast fracture angle is 90°, the fracture volumetric strain remains relatively constant with increasing the axial strain under different confining pressures. While, when the precast fracture angle is 80°, the fracture volumetric strain shows a slight contraction with the increase in the axial strain. The increment values of fracture volumetric strain in the elastic stage under confining pressures of 15~35 MPa are as follows: 0.02, 0.035, 0.031. When the precast fracture angle is 70°, the fracture volumetric strain exhibits a pronounced contraction with varying degrees. The contraction incremental values under different confining pressures are: 0.079, 0.106, and 0.14, respectively. In the stable propagation stage of fractures (BC), with the increase of precast fracture angle, the fracture volumetric strain changes from contraction to expansion, and this effect becomes more pronounced

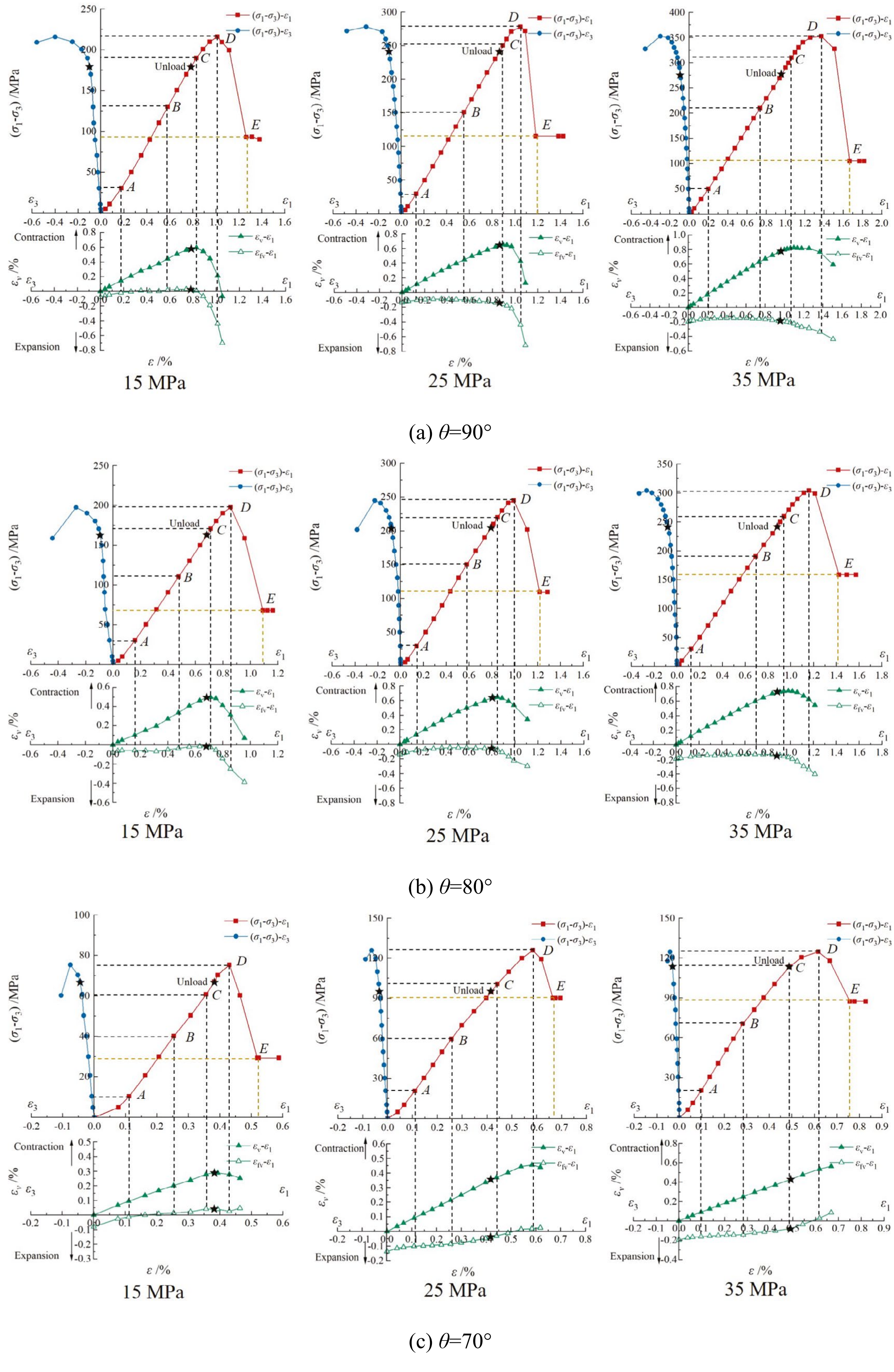

Fig. 5 Stress–strain curve and volumetric strain-axial strain curve of the penetrating fractured rock mass

with decreasing confining pressure due to the expansion of micro-fractures and the deformation of precast fractures. In the rapid propagation stage of fractures (CD), all samples transfer from the loading to the unloading phase. Both rock and fracture volumetric strain exhibited a clear nonlinear development trend, showing overall expansion. However, the degree of expansion decreased with increasing the confining pressure. The development of new fractures and the deformation of precast fractures together cause the rock mass to exhibit the most substantial expansion when the precast fracture angle is equal to 90°. Furthermore, when the precast fracture angle is 80°, the variation law of volumetric strain in both rock and fracture are similar to those of the 90° precast fracture rock mass while the degree of expansion is smaller than the former case. This is primarily because, with increasing the axial load, the normal stress on the fracture face restricts the expansion deformation of the fracture to some extent. However, the normal force is still relatively small, in which leads the fracture strain to show a continues volumetric expansion. When the precast fracture angle is 70°, under low confining pressure, both the rock volumetric strain and fracture volumetric strain still exhibit a slight volumetric expansion. However, with increasing the confining pressure, there will be a shift in the volumetric strain from expansion to contraction. This is because, at this fracture angle, the axial load significantly increases the normal force on the rupture plane. which leads to a more pronounced closure effect on the fracture. Additionally, with increasing the confining pressure, the rock mass, under the same stress state, experiences higher axial stress, resulting in a stronger closure effect on the fracture. Therefore, under high confining pressure, it exhibits volumetric contraction.

Figure 6 shows the precast fractured rock masses' elastic modulus and Poisson's ratio fluctuation curves. The elastic modulus and Poisson's ratio of the rock mass show a significant decrease in comparison with the intact rock. However, as the fracture angle and confining pressure increase, the differences in elastic modulus and Poisson's ratio between the fractured rock mass and intact rock decrease. The relationship between the elastic modulus and Poisson's ratio of fractured rock mass and the confining pressure can be approximated by quadratic equations. Figure 7 shows a comparison

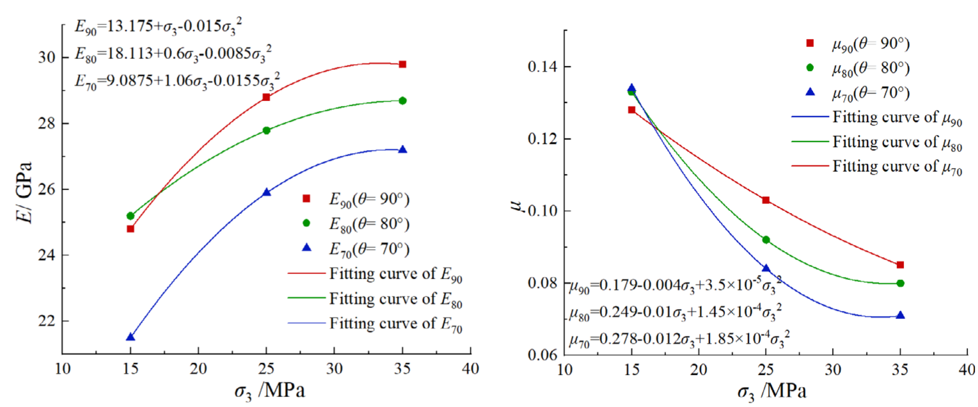

(a) Variation curves of elastic modulus (b) variation curves of Poisson's ratio

Fig. 6 Precast fractured rock masses' elastic modulus and Poisson's ratio fluctuation curves

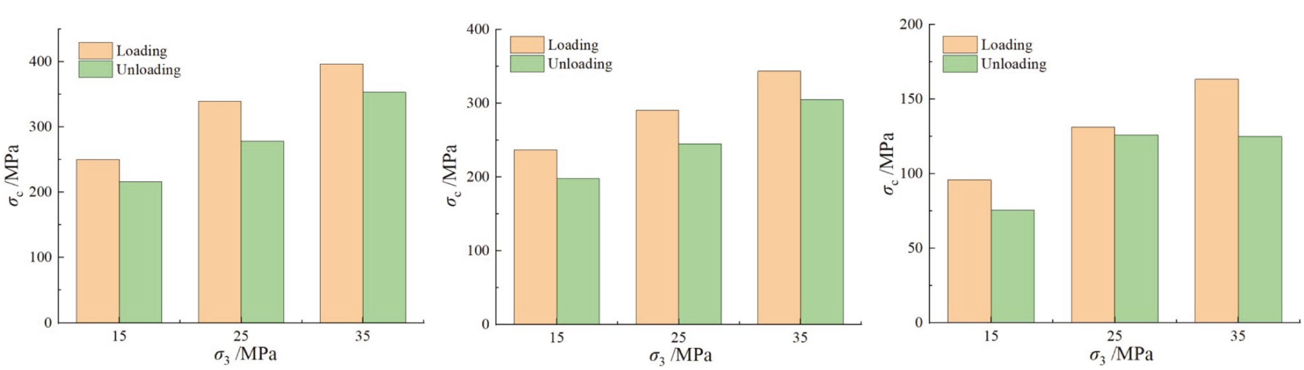

(a) θ=90° (b) θ=80° (c) θ=70°

Fig. 7 Comparison of peak strength under triaxial loading and unloading conditions between peak stress under loading and unloading conditions for the rock mass. Under the influence of precast fracture angle 90°~70°, the peak strength of the rock mass under unloading conditions decreases by approximately 86.4~89.1%, 83.5~88.7%, and 78.8~76.4%, respectively, compared to the loading conditions with the decreasing of precast fracture angle. In general, under unloading conditions, as the fracture angle decreases, the reduction degree in rock strength gradually increases in comparison with loading conditions. While the reduction degree decreases with increasing the confining pressure.

3.2 Failure Mode of Fractured Rock Mass Under Loading and Unloading Conditions

Figure 8 illustrates the evolution of failure modes under the influence of precast fracture angles and confining pressures. The type of failure in fractured rock masses is influenced not only by the strength of the rock material but also by the presence of structural surfaces (Ma et al. 2024; Ansari et al. 2020). The fractures generated within the material are regarded as material failure, while the fractures extending from precast fractures are regard as a structural failure. The rock mass failure types under different confining pressures and fracture angles are presented in Table 3. When the precast fracture angle is 90°, the rock undergoes material failure, characterized by shear failure mode where the rupture plane penetrates the entire specimen. While, when the precast fracture angle is 80° or 70°,

Table 3 Type of rock mass failure

Confining pressure /MPa	Precast fracture angle		
	70°	80°	90°
15	Structural failure	Structural failure	Material failure
25	Structural failure	Structural failure	Material failure
35	Structural failure	Structural failure	Material failure

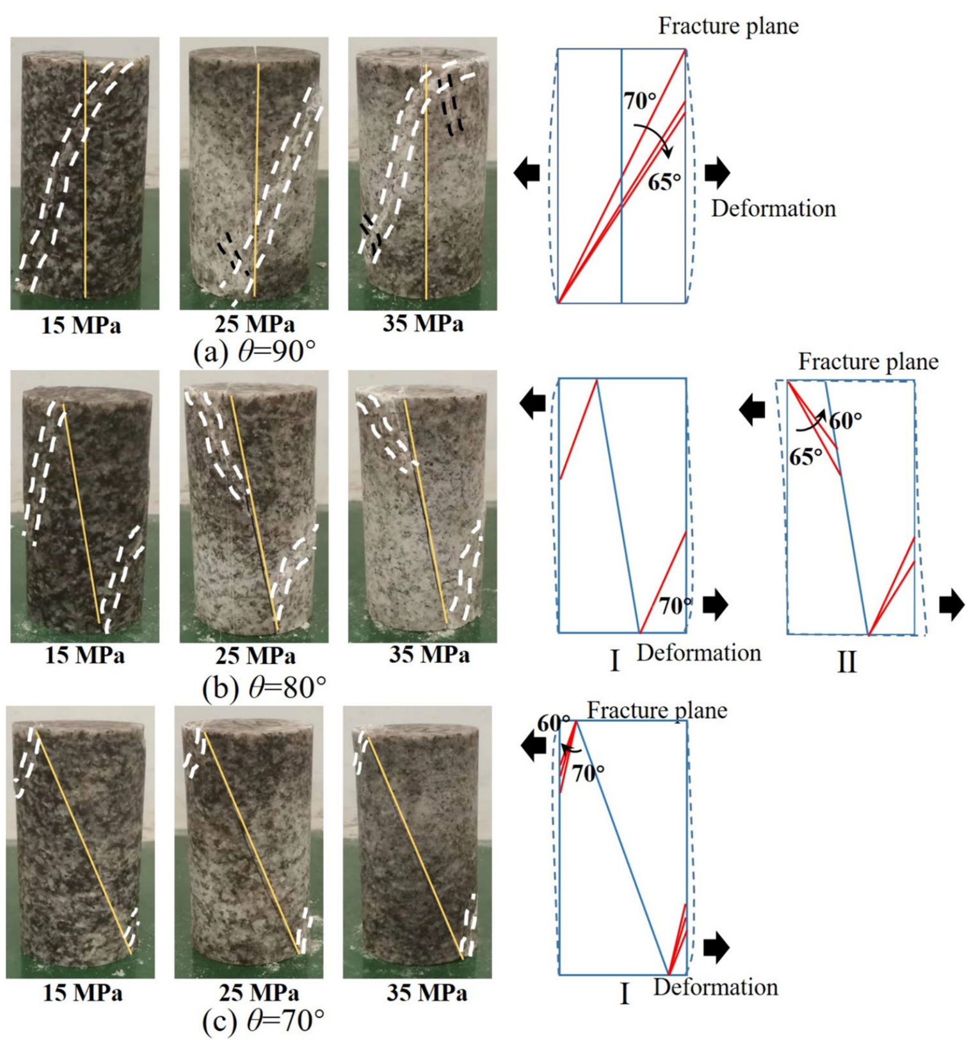

Fig. 8 Evolution of failure modes under the influence of precast fracture angles and confining pressures (The white line represents shear failure, while the black line represents tensile failure)

the rock failure type is structural failure, with localized shear failure occurring at the ends of the specimen.

At a precast fracture angle of 80°, the rock failure mode shifts from localized failure mode I to localized failure mode II due to an increase in the confining pressure. Localized failure mode I appears as shear failure slipping surfaces from the precast fracture end towards the outer side of the specimen. This is mainly due to stress concentration at the specimen end under the action of axial load when the confining pressure is relatively low, which leads to an increase in the damage on the thinner side of the specimen end. Thus, the subsequent deformation expands towards the σ_3 direction, resulting in the extension of the rupture plane outward. Under the influence of high confining pressure, localized failure mode II primarily involves the development of shear failure surfaces on the upper side towards the direction of the precast fracture, while the lower side of the specimen still exhibits shear failure surfaces slipping from the precast fracture towards the outer side of the specimen. This is partly due to the significant inhibitory effect of high confining pressure on the lateral deformation of the rock mass. Consequently, under axial loading, the specimen's end will be exposure to a shift from expansion deformation to bending deformation on σ_3 direction. On the other hand, the upper part of the specimen which is the gas inlet end, experiences more significant lateral thrust from the gas against the fracture face during unloading, leading to a more pronounced bending effect. Therefore, the contact force on the upper part of the precast fracture is relatively smaller than that on the lower part. As a result, the shear failure surface develops towards the side of the precast fracture in the upper part. While, the lower part, where the gas pressure inside the fracture is minimal, has a less noticeable impact on the rock mass deformation. Moreover, the rupture plane still develops towards the outer side. When the precast fracture angle is 70°, the rock mass failure mode is consistently local failure mode I. This is because, under the condition of a 70° precast fracture angle, stress concentration at the end of the specimen is more pronounced, leading to a more significant expansion phenomenon on σ_3 direction at the end of the specimen. In addition, the axial load before the failure of the rock mass is relatively low, which prevents the occurrence of significant bending deformation.

Further analysis reveals that the angle between the rock mass rupture plane and the major principal stress decreases with increasing confining pressure. When the precast fracture angle is 90°, the angle between the rupture plane and the major principal stress decreases from 70° to 65° as the confining pressure increases from 15 to 35 MPa. For precast fracture angles of 80° and 70°, the angle between the rock mass rupture plane and the major principal stress decreases from 70° to 60° with increasing confining pressure. Overall and after considering the previous results, the effect of confining pressure on the angle between the rock mass rupture plane and the major principal stress will increase with each decrease in the precast fracture angle.

3.3 The Permeability Characteristics of Fractured Rock Mass

Figure 9 illustrates the permeability variation curve of fractured rock mass during the loading and unloading processes, where η represents the slope of the permeability changing curve. Taking 15 MPa confining pressure as an example, the permeability variation curves of the rock mass under different precast fracture angles during the loading and unloading processes are analyzed. When the precast fracture angle is 90°, the permeability curve initially decreases slightly, and then increases with increasing the deviatoric stress. The stress state of the rock mass is mostly in the stable propagation stage of fractures in the loading phase, and there is a limited expansion deformation. The fracture aperture is less affected by deviatoric stress. Therefore, during the loading phase, the permeability of the rock mass increases slowly with the increase in the deviatoric stress, and the slope of the curve remains relatively constant. The permeability of the rock mass during the loading phase only increases by about 2.5% in comparison with the initial stress. When the rock mass is in the unloading phase, the reduction in the confining pressure reduces the normal stress on the fracture surfaces. Furthermore, the rock mass assumes a rapid propagation stage of fractures, and the volume strain expansion becomes pronounced, leading to an increase in fracture aperture. Therefore, during the unloading phase, the slope of the permeability curve exhibits a significant nonlinear increase with each increase in deviatoric stress. Under peak stress, the permeability of the rock mass increases by approximately 10.2% in comparison with the initial stress. When the precast fracture angle is 80°, the permeability curve shows a law of initially decreasing and then increasing with the increase in deviatoric stress. During the early stages of loading, the rock undergoes elastic deformation. The increase in deviatoric stress not only causes an increase in normal stress on the fracture surfaces, leading to significant closure of rock fractures but also increases the degree of stress concentration at the end of the specimen. The rock at the end undergoes expansion due to stress concentration, but the extent of expansion is still limited because the area affected by stress concentration is small. Consequently, when the axial stress increases, the permeability, which had first decreased, gradually will tend to increase. During the loading phase, the rock permeability increases by approximately −5.7% in comparison with the initial stress. When the rock mass is unloaded, the permeability increases rapidly with the increase in deviatoric stress. This is because the reduction in confining pressure directly lowers the normal

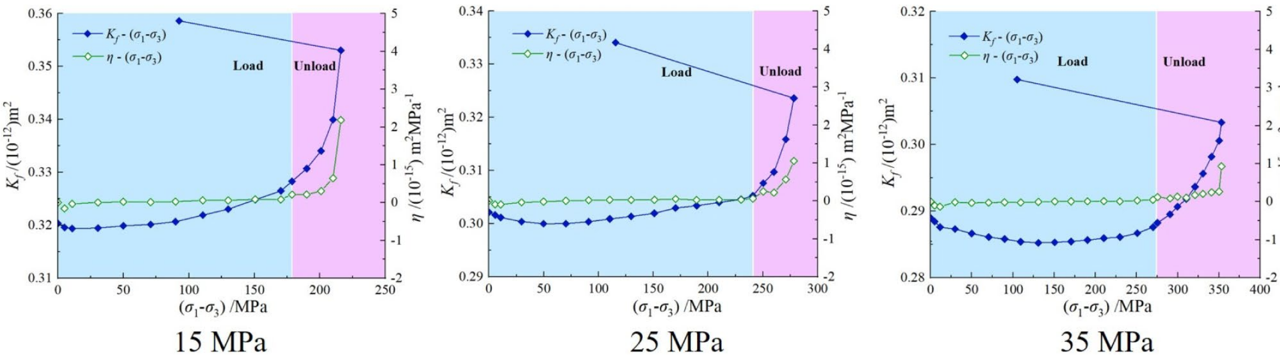

(a) θ=90°

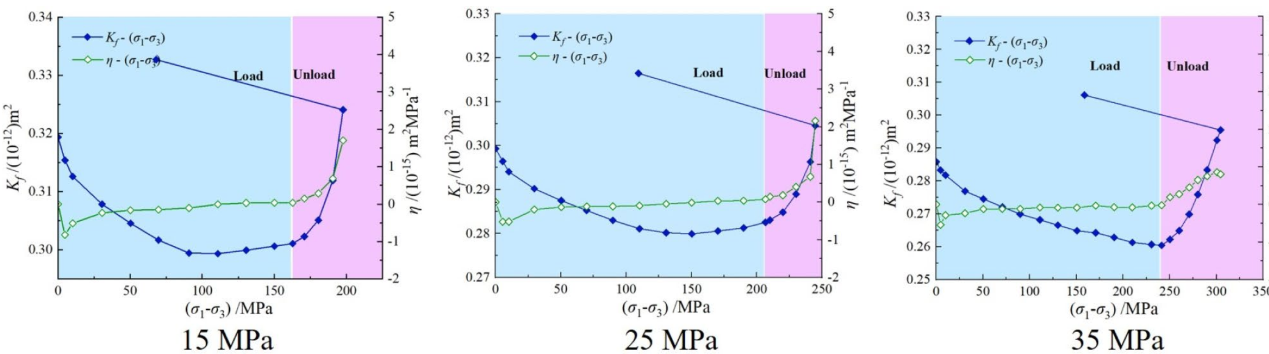

(b) θ=80°

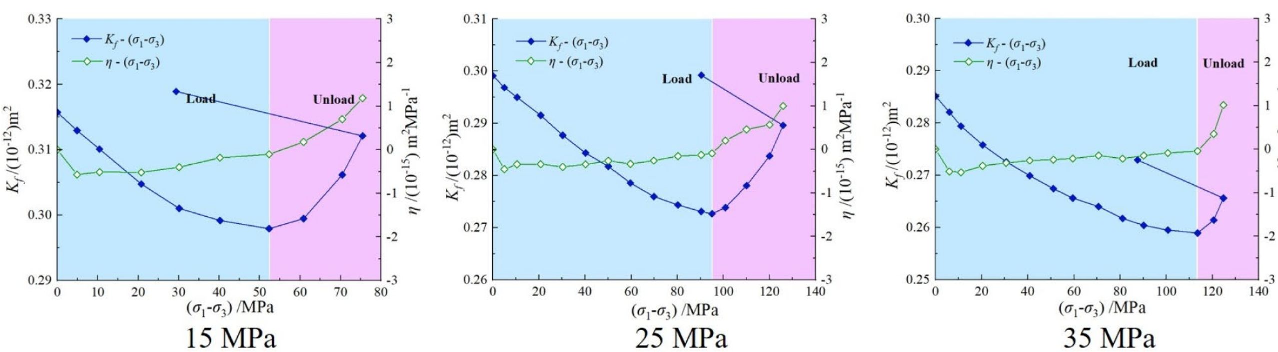

(c) θ=70°

Fig. 9 Permeability variation curve of fractured rock mass during the loading and unloading processes

stress on the fracture surfaces. Moreover, as the confining pressure decreases, the damage at the end of the specimen increases which leads to expansion contribution. Therefore, during this phase, the permeability curve exhibits nonlinear growth, but the increase is still smaller than that of a 90° precast fracture rock mass case. The permeability under peak stress state increases approximately by 1.5% in comparison with the initial stress. Therefore, during this stage, the permeability curve exhibits nonlinear growth, but the increase is smaller than that of a 90° fracture. The permeability under peak stress increases by approximately 1.5% in comparison with the initial stress. The permeability curve of the 70° precast fracture rock mass follows a similar law to that of the 80° precast fracture rock mass. However, due to the more significant influence of the deviatoric stress on the normal stress of the fracture surface, the permeability of the rock mass during the loading phase always shows a decreasing trend. The permeability during the loading phase increases by approximately −5.6% in comparison with the initial stress. During the unloading phase, the change in the normal stress component on the fracture surface due to the decrease in confining pressure is relatively small, and the limited degree of deformation of the rock mass at the end contributes to only a slight increase in permeability with the increase in deviatoric stress. The permeability under peak stress increases by approximately −1.1% in comparison with the initial stress.

Taking 70° fractured rock mass as an example, the permeability curve of rock mass under different confining pressures is analyzed. The permeability of the whole rock mass exhibits a law of decreases first and then increases with the increases in deviating stress. However, the inhibition effect of deviating stress on the permeability of rock mass increases with the increase of confining pressure. The rock permeability during the loading phase increases by approximately −5.6, −8.8, and −9.2% compared to the initial stress. The degree of rock mass expansion decreases during the unloading phase, leading to a reduction of the enhancement effect on rock mass permeability by unloading. During the unloading phase, the permeability increases by approximately −1.1, −3.2, and −6.8% in comparison with the initial stress.

The curves in Fig. 10 represent the variations in permeability and Reynolds number under different stress states. The Reynolds number (Re) is an important parameter characterizing fluid flow characteristics, providing a comprehensive reflection of the relationship between fluid flow state, viscosity, fracture geometry, and flow velocity. The Reynolds number is calculated by Eq. (7) (Lee et al. 2014). At different stress states, the permeability of fractured rock mass approximately decreases linearly with the increase in the confining pressure. Under the same stress states and confining pressure, the permeability increases with the increase in precast fracture angle. Moreover, as the stress state increases, the differences in permeability among different precast fracture angles become more pronounced. Taking 15 MPa confining pressure as an example, when the fracture angle decreases from 90° to 70°, the permeability of rock mass in initial stress and peak stress decreases by about 1.2 and 11.6% respectively. Following the failure stage, the enhancement effect of rock permeability increases with the decrease in precast fracture angle. As the precast fracture angle decreases from 90° to 70°, the post-failure rock mass permeability increases by approximately 1.7, 2.8, and 2.2% in comparison with the initial stress.

The Reynolds number (Re) can reflect different flow states of the fluid. Under the experimental conditions, the Reynolds number of CO_2 in fracture rock mass is less than 10, indicating that the flow is in a linear laminar state. The Reynolds number variation law is similar to the permeability. With the decrease in the confining pressure and the increase in precast fracture angle, the trend of fluid flow state gradually transitions from linear laminar to nonlinear laminar development, especially when the rock is in the unloading phase, the Reynolds number exhibits the most significant changes.

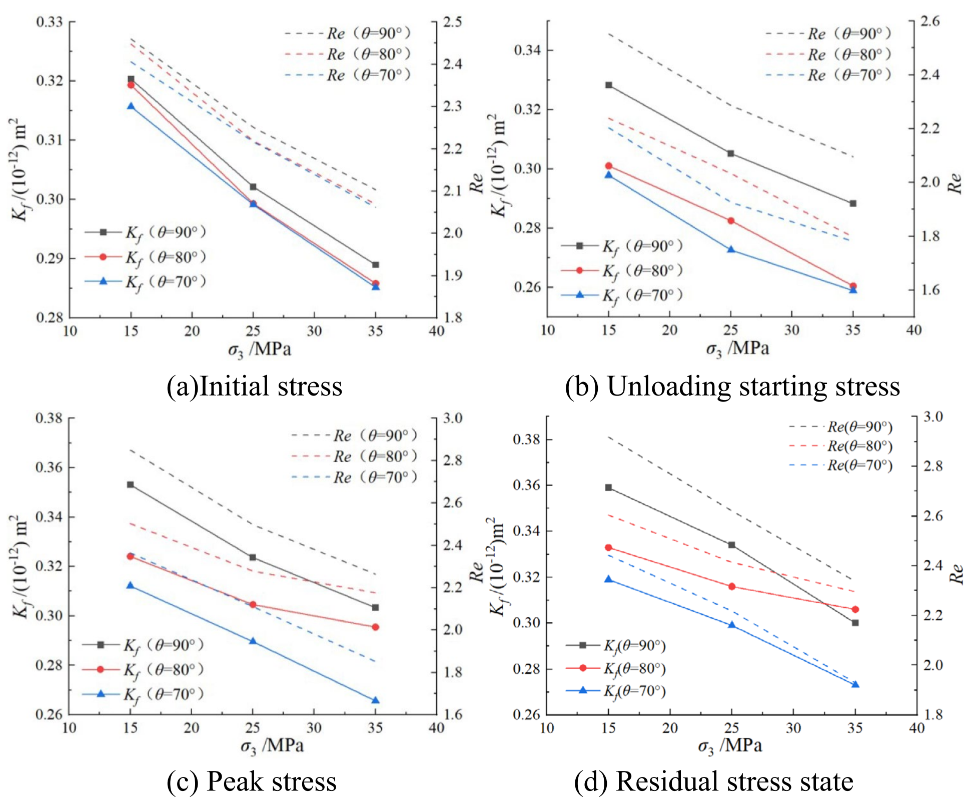

Fig. 10 Variation curves of permeability and Reynolds number of fractured rock mass under different stress states

$$\mathrm{Re} = \frac{\rho v e_n}{\mu_g} = \frac{\rho_g Q}{\mu \omega} \tag{7}$$

where Re is Reynolds number, ρ_g is fluid density (kg/m^3), Q is the fluid flow rate (m^3/s), μ_g is the dynamic viscosity of the fluid (Pa·s), υ is the kinematic viscosity of the fluid (m^2/s), d_f is equivalent hydraulic aperture (m), ω is the width of the fracture (m).

4 Fluid–Solid Coupling Model of Fractured Rock Mass

4.1 Governing Equation of Fluid–Solid Coupling Model

According to generalized Hooke's law, the constitutive equation of rock mass under fluid–solid coupling is as follows (Lei et al. 2021; Ma et al. 2023b):

$$Gu_{i,jj} + \frac{G}{1-2\mu}u_{j,ji} + \alpha p_{,i} + F_i = 0 \tag{8}$$

where G is the shear modulus of the rock, $G = E/[2(1+\mu)]$, F_i and u_i ($i = x$, y, z) are the components of force and displacement in the i direction, p_i is the component of seepage pressure in the i direction, α is Biot's coefficient.

Seepage in fractured rock mass includes porous media seepage and fracture seepage. The flow equation satisfies the conservation of mass and Darcy law. The matrix seepage equation is as follows:

$$\frac{\partial\left(\rho_g \phi\right)}{\partial t} + \nabla \cdot \left(\rho_g U\right) = Q_m - \rho_g \alpha \frac{\partial \varepsilon_v}{\partial t} \tag{9}$$

where ρ_g is the fluid density, Φ is the rock mass porosity, t is time, U is flow velocity, Q_m is the source term.

The seepage equation of fracture medium in the rock mass is as follows:

$$d_f \frac{\partial\left(\rho_g \phi_f\right)}{\partial t} + \nabla \cdot \left(d_f \rho_g U\right) = d_f Q_m - d_f \rho_g \alpha \frac{\partial \varepsilon_v}{\partial t} \tag{10}$$

where Φ_f is the fracture porosity.

Seepage velocity in rock mass can be calculated as the following:

$$U = -\frac{k}{\mu_g}\nabla p \tag{11}$$

where k is the permeability of rock mass.

4.2 Damage Evolution Equation

Maximum tensile stress criterion and M-C criterion (Eq. 12) are used to distinguish rock mass damage. When the tensile stress of rock mass exceeds the tensile strength of rock mass ($F_1 > 0$), the rock mass will suffer tensile damage. While, when the shear stress reaches the M-C yield surface ($F_2 > 0$), the rock mass will suffer shear damage. The calculation method of damage amount is shown in Eq. (13).

$$\begin{cases} F_1 = -\sigma_3 - f_{t0} \\ F_2 = \sigma_1 - \sigma_3 \frac{1+\sin\varphi}{1-\sin\varphi} - f_{c0} \end{cases} \tag{12}$$

where F_1 and F_2 are the state functions of tension and shear stress, f_{t0} is the uniaxial tensile strength, f_{c0} is the uniaxial compressive strength, φ is the internal friction angle of the rock mass.

$$D = \begin{cases} 0 & F_1 < 0 \ F_2 < 0 \\ 1 - \left|\frac{\varepsilon_{t0}}{\varepsilon_3}\right|^n & F_1 = 0 \ \mathrm{d}F_1 > 0 \\ 1 - \left|\frac{\varepsilon_{c0}}{\varepsilon_1}\right|^n & F_2 = 0 \ \mathrm{d}F_2 > 0 \end{cases} \tag{13}$$

where ε_{t0} and ε_{c0} are the maximum principal strains corresponding to tensile damage and shear damage, respectively. n is the damage evolution coefficient, and the higher the value, the more obvious the brittle failure characteristics. In this paper, $n = 2$ is taken. D is the damage amount. When $F_1 < 0$ and $F_2 < 0$, no damage occurred in rock mass. When $F_1 \geq 0$ or $F_2 \geq 0$, and $\mathrm{d}F_1 > 0$ or $\mathrm{d}F_2 > 0$, the rock mass is in the loading state and the damage amount continues to increase. When $\mathrm{d}F_1 \leq 0$ or $\mathrm{d}F_2 \leq 0$, the rock mass is in the unloading state, and the damage does not change.

4.3 Effects of Damage on Fluid–Solid Coupling Parameters

According to the elastic damage theory, the relationship between the elastic modulus and damage is as follows:

$$E = (1-D)E_0 \tag{14}$$

where E_0 is the initial elastic modulus of the material.

The porosity of rock mass in the elastic stage is mainly related to the stress state of rock mass, while when the rock mass enters the plastic deformation stage, the porosity of rock mass increases significantly with the increase of damage amount (Hamiel et al. 2004). The internal structure of granite is relatively dense and its natural porosity is very low. Therefore, regardless of the compression effect of stress on natural pores, the change in granite porosity is mainly caused by the damage to the rock matrix. The relationship of porosity with damage can be expressed as the following:

$$\phi=\phi_0 + D\left(\phi_r - \phi_0\right) \tag{15}$$

where Φ_0 is the initial rock mass porosity, Φ_r is the rock mass porosity after failure.

The evolution of rock permeability with porosity after damage is as follows:

$$k = k_0\left(\frac{\phi}{\phi_0}\right)^3 e^{\alpha_k D} \tag{16}$$

where α_k is the stress sensitivity coefficient of the porosity, 5×10^{-8} Pa^{-1} is taken (Liu et al. 2020).

4.4 Calculation Model of Fracture Permeability

The normal stress of the fracture surface is the most important factor affecting the fracture aperture. Thus, the previous studies were mostly carried out around the influence of normal stress, and the closure amount of the fracture surface under the action of normal stress which is usually calculated according to the following equation:

$$\Delta d_f = d_{f0}\left(1 - e^{-\frac{\sigma_n}{k_n}}\right) \tag{17}$$

where σ_n is the normal stress of the fracture surface and k_n is the normal stiffness.

By equating the lateral stress to the normal tension stress of the fracture surface, Liu and Chen (2007) established an equivalent hydraulic aperture calculation method considering the normal and lateral stress of the fracture surface under fluid–solid coupling conditions.

$$d_f = d_{f0}e^{-\frac{\sigma_3-\chi(\sigma_1+\sigma_2)-p}{k_n}} \tag{18}$$

where χ is the lateral stress influence coefficient on normal deformation.

Based on previous research, it is known that there are certain differences in the deformation characteristics of fractures in the rock mass under different stress levels. In general, with higher stress levels, the influence of lateral stress on fractures becomes more significant. Therefore, the calculation of fracture aperture under fluid–solid coupling can be modified as the following:

$$d_f = d_{f0}e^{-\lambda\frac{\sigma_n-\chi K_i\sigma_\tau-p}{k_n}} \tag{19}$$

where K_i is the stress level, λ is the coefficient of fluid properties. When $\sigma_2=\sigma_3$, under the influence of different precast fracture angles, the normal stress σ_n and lateral stress σ_τ of the fracture surface are expressed as follows:

$$\begin{cases} \sigma_n = \sigma_3\sin\theta + \sigma_1\cos\theta \\ \sigma_\tau = \sigma_3(1+\cos\theta) + \sigma_1\sin\theta \end{cases} \tag{20}$$

5 Results of Numerical Simulation

5.1 Model Establishment and Validation

The damage of rock is related to the stress state, and the seepage state of fluid in rock mass is related not only to the seepage pressure and stress state, but also to the seepage time. Therefore, numerical calculations for rock damage are often performed under steady-state simulations, while the fluid state changes within the fractures require transient simulations. Figure 11 depicts the coupled fluid–solid numerical simulation method for fractured rock masses considering damage and seepage time effects by using COMSOL software. The calculation steps are as follows: first, seepage pressure and stress boundary conditions are added for steady-state calculation to obtain the damage field and stress field of the rock mass. Then, to calculate the damage degree and the evolution of the seepage state during the compression process, the damage field and stress field are introduced into transient calculation. Furthermore, the boundary conditions such as the seepage field of the previous transient calculation step and seepage time increment were added.

The model size and the boundary conditions are shown in Fig. 12. Part of the calculated parameters are shown in Table 4. The initial elastic modulus E_0 and Poisson's ratio μ of rock mass under different confining pressures can be calculated by using the fitting equations obtained from Fig. 6. The elastic modulus within the rock follows Weibull distribution.

The numerical simulation parameters for permeation calculation, including χ, λ, and K_i, were obtained by reverse calculation of the permeability curve from comparative experimental data. The specific method is as follows: (1) The permeability calculation parameters χ and λ are first obtained through the proposed methods. (2) The axial stress during the loading and unloading process is monitored to obtain σ_i. The axial stress during the loading process is monitored to obtain σ_i. The stress level, obtained from the stress σ_i obtained from numerical simulation divided by the peak stress σ_c obtained from experiments. (3) Conduct fluid–solid coupling calculations to obtain the variation curve of permeability K_f. (4) The permeability curve K_f that has been obtained from the results of the numerical simulation is compared with the experimental curve. Where there is a high degree of agreement between the numerical simulation curve and the experimental curve, the obtained values of χ and λ were considered correct. If there is a significant

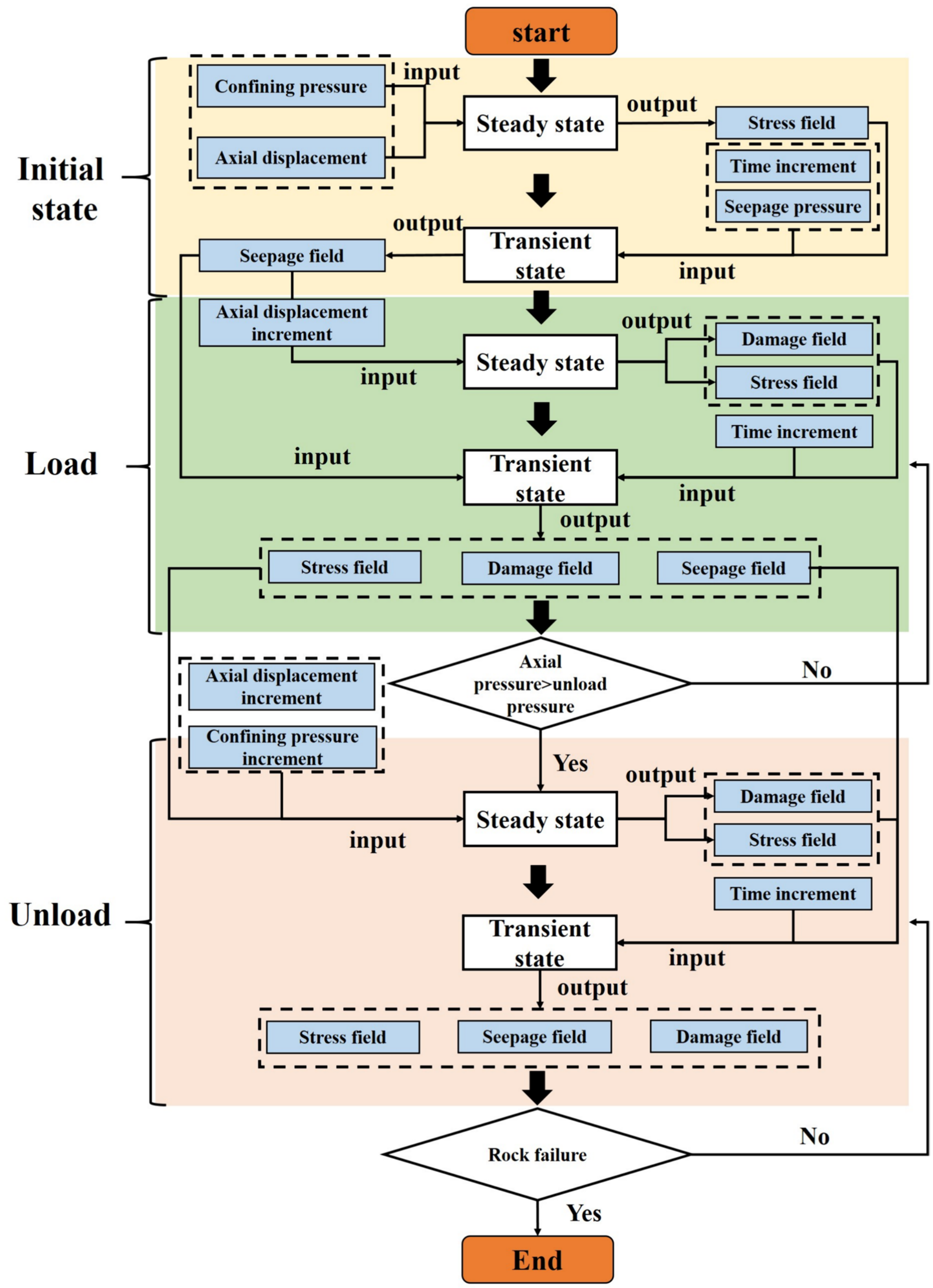

Fig. 11 Calculation process of numerical simulation

discrepancy between the numerical simulation curve and the experimental curve, the process returns to step (1) for further calculation until the suitable requirement.

Table 5 presents a comparison between the experimental and numerical simulation strengths of the rock mass. The error between the numerical simulation and the measured value is within 10% under different confining pressures and fracture angles. For further comparison between the deformation and permeation evolution laws under different confining pressures and fracture angles, the stress–strain curves and permeability change curves obtained from the numerical simulations and the experiments are plotted in Fig. 13. Upon the comparison, it is found that both the stress–strain curves and the permeability changing curves show a high degree of agreement between the numerical simulation and experimental data. Upon comparing the stress–strain curves, it is observed that the numerical simulation exhibits initial strain linearly increasing with stress. However, the strain exhibits a nonlinear increase with the stress during the unloading phase because of the increased damage. When the confining pressure increases, the permeability development curves of the rock mass are compared, and it is found that overall

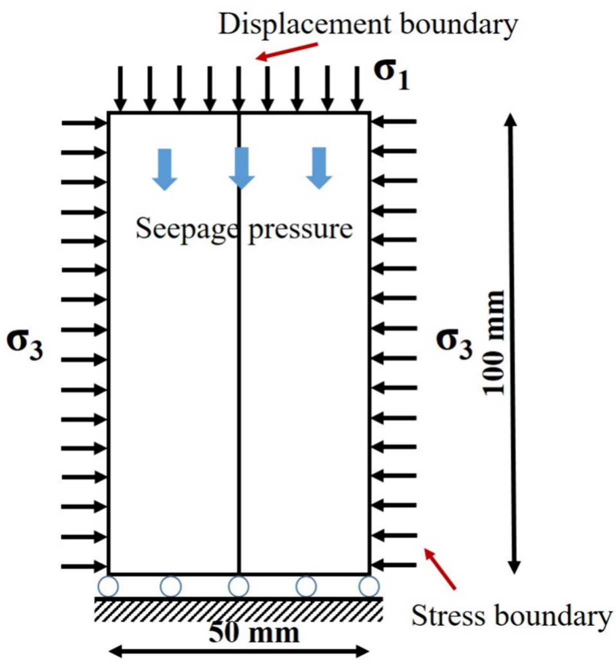

Fig. 12 Model size and boundary conditions

permeability decreases. There are differences in the permeability variation under different fracture angles. The total permeability of the rock mass increases as the axial stress increases when the fracture angle is 90°, and this increase in permeability is most noticeable during the unloading phase. However, when the fracture angles are 80° and 70°, the permeability of the rock mass initially decreases and then increases with increasing the axial stress. The increase in permeability is the most pronounced feature during the unloading phase. In summary, the deformation and permeation variations obtained from numerical simulations are generally consistent with the experimental findings. This indicates that the damage-permeation evolution characteristics of rock masses under various confining pressures and fracture angles can be accurately reflected by the numerical model that takes into account the influence of lateral stress on fracture surfaces in rock mass fluid–solid coupling calculations.

Figure 14 shows the variation curve of the lateral stress influential coefficient on the normal deformation χ with the confining pressure. Under different precast fracture angles, the lateral stress influential coefficient on the normal deformation χ of rock mass decreases slowly with increasing the confining pressure. Moreover, the increment of decrease diminishes as the confining pressure increases. Under the same confining pressure, χ decreases rapidly with the increase of precast fracture angle, and the effect of fracture angle on χ is much greater than that of confining pressure. It shows that with the decrease of the fracture angle, the lateral stress has a significant effect on the fracture opening due to the bending deformation of the end of the specimen. Additionally, the normal deformation brought on by the lateral stress on the fracture is somewhat inhibited by the confining pressure; nevertheless, the sensitivity of the confining pressure to the normal deformation brought on by the lateral stress is significantly less than the fracture angle.

Furthermore, the fitting curve process reveals that the variation curve of χ with the confining pressure follows a

Table 4 Numerical simulation parameters of fluid–solid coupling

Strength parameters	Value	Seepage parameters	Value
Uniaxial tensile strength f_{t0}	5 MPa	Initial rock mass porosity Φ_0	0.005
Uniaxial compressive strength f_{c0}	144 MPa	Maximum rock mass porosity Φ_r	0.6
Internal friction angle φ	56°	Fracture porosity Φ_f	0.8
Biot's coefficient α	0.8	CO_2 initial density ρ_g	70 kg/m^3
Normal stiffness k_n	45 GPa	Dynamic viscosity of the fluid μ_g	1.46e−5 Pa·s
		Initial permeability of rock mass K_0	1e−19 m^2
		Initial permeability of fracture K_{f0}	0.352e−12 m^2
		Coefficient of fluid properties λ	240

Table 5 Comparison between experimental and numerical simulation in rock strengths

Confining pressure /MPa	Precast fracture angle					
	70°		80°		90°	
	Simulation /MPa	Experiment /MPa	Simulation /MPa	Experiment /MPa	Simulation /MPa	Experiment /MPa
15	74.67	75.43	182.49	197.63	208.26	216.04
25	120.07	125.90	249.83	244.80	279.20	278.26
35	129.07	124.70	303.89	304.40	340.94	353.04

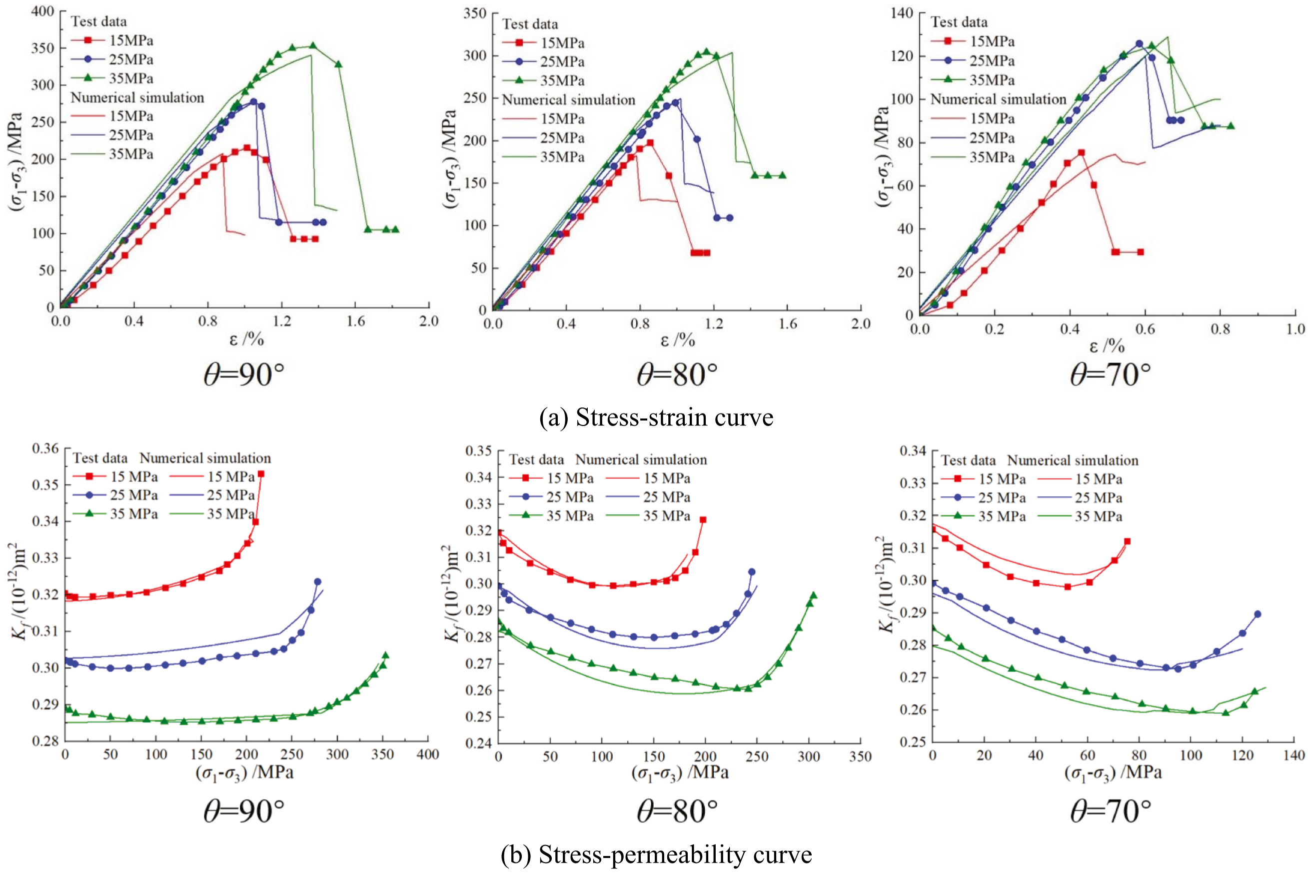

Fig. 13 Comparison between numerical simulation and experiment

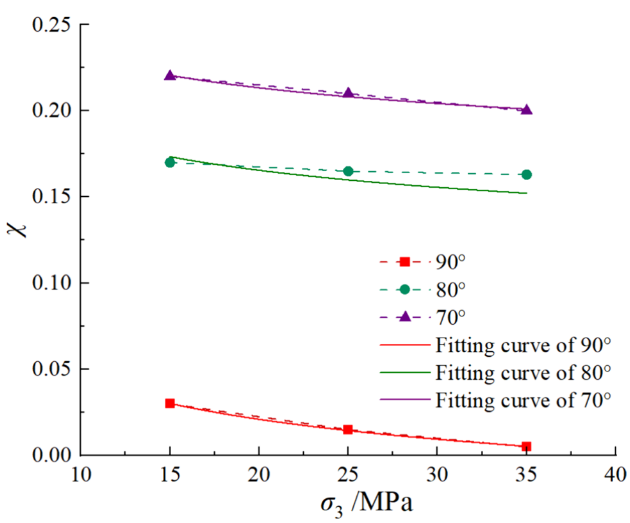

Fig. 14 Variation curve of χ with confining pressure

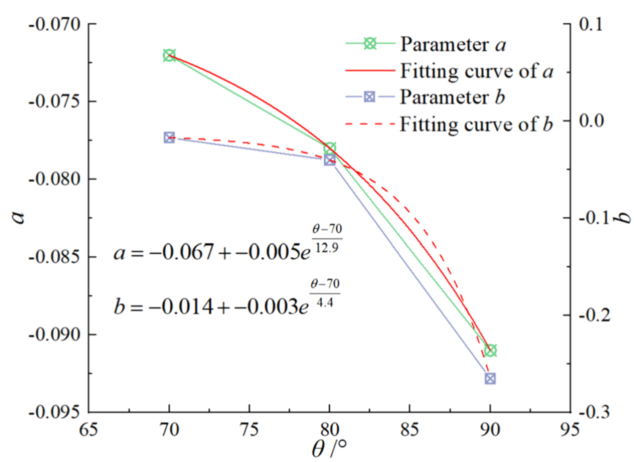

Fig. 15 Fitting curve of parameters

logarithmic function distribution, expressed in Eq. (21). Figure 15 displays the variation of fitting parameters with the fracture angle. The results show a nonlinear increasing trend for both parameters a and b with increasing fracture angle. To quantitatively express the relationship between parameters a and b and the fracture angle, their variation trends were fitted by using an exponential function. The variation of parameters a and b with the fracture angle can be calculated by using Eq. (22).

$$\chi = a \ln\left(-b \ln\left(\sigma_3\right)\right) \tag{21}$$

$$\begin{cases} a = -0.067 - 0.005e^{\frac{\theta-70}{12.9}} \\ b = -0.014 - 0.003e^{\frac{\theta-70}{4.4}} \end{cases} \tag{22}$$

5.2 Damage Evolution During Loading and Unloading Process

To clarify the damage evolution during the loading and unloading process of fractured rock masses, taking 35 MPa confining pressure as an example, the analysis of rock damage evolution under different fracture angles is conducted. Select the initial stress (σ_0), unloading start stress (σ_u), peak stress (σ_c), and residual stress (σ_{cr}) respectively to draw the damage field in the rock mass. Plot the damage amount $\sum D$ variation curve with axial strain ε_1 to quantitatively examine the variation of rock damage during the loading and unloading process in Fig. 16, where $\sum D$ is the damage values of all grid nodes in the model added together. Under the influence of different precast fracture angles, no obvious damage occurs in the rock mass before unloading. When the peak stress is reached, a large number of damage units are generated in the rock mass, and the damage units are mostly concentrated around the potential shear rupture plane. When the rock mass enters the state of residual stress, the rock mass is damaged and the amount of damage $\sum D$ reaches the maximum.

Further analysis of the rock damage curve during the loading and unloading process reveals that when the precast fracture angel is 90°, the damage amount is basically unchanged with the increase of axial strain at first. When the axial strain approaches the peak strain, the damage amount of rock mass shows a sudden increase. Under peak stress, the damage amount of rock mass is about 6000, while after the rock mass failure, the damage amount reaches 2.77e6. When the precast fracture angle is 80°, the damage amount of rock mass first presents a linear increase trend with the increase of axial strain. When the rock mass enters the unloading phase, the slope of the damage amount curve increases. However, the trend of the curve is still linear. When the axial strain approaches the peak strain, the curve presents a nonlinear increase trend, and the damage amount is 4376 at the peak stress and 2.31e6 at the residual stress. When the precast fracture angle is 70°, the variation law of the damage amount curve is similar to that of the 80° precast fracture condition. However, when the rock mass starts unloading, the damage curve immediately exhibits a significant nonlinear growth trend. The damage amount is 18,226 at peak stress and 8.46e5 at the residual stress. By comparing the damage amount of the rock mass under the same stress state, it is observed that before the rock mass failure, the degree of damage inside the rock decreases with the reduction of the precast fracture angle. After the rock mass failure, the larger the precast fracture angle, the greater the degree of damage within the rock mass. This is mainly because, with the reduction of the precast fracture angle, the stress concentration at the specimen's end becomes more pronounced, leading to earlier damage in the rock mass during the compression process while the stress concentration area also decreases relatively with the reduction of the fracture angle, leading to smaller damage amount zone after failure.

5.3 Seepage Evolution During Loading and Unloading Process

Figure 17 shows the permeability evolution of the rock mass with different precast fracture angles under the influence of a confining pressure of 35 MPa. To quantitatively analyze the changing permeability in the rock masses, the permeability of the whole calculation elements of the rock matrix is averaged, and the relation curve of the average permeability Φ_a with axial strain ε_1 is obtained. The development trend of average permeability with axial strain is basically consistent with the damage. In the case of a 90° precast fracture angle, the maximum average permeability after rock failure is 1.99e−14 m^2. As the fracture angle decreases, the post-failure rock permeability also decreases, with average permeabilities of 2.13e−14 and 2.39e−15 m^2 for 80° and 70° precast fractures angle, respectively.

To analyze the flow state of CO_2 in the rock matrix and fractures during the loading and unloading process, the seepage velocity and pressure evolution of the fractured rock mass under different stress conditions are depicted in Fig. 18. For granite dense rock mass, most of the seepage pressure only acts on the rock surface, the seepage pressure in the rock decreases rapidly with the increase of depth. Analysis of fluid flow velocity and gas pressure distribution in the rock under different stress states indicates that before the rock is damaged, the increase in rock permeability is not significant due to the small degree of damage inside the rock. Moreover, fluid seepage during the compression process lags behind the damage variation, and the evolution of gas seepage has not reached an equilibrium state. Therefore, the gas flow velocity and pore pressure within the rock show relatively small variations with axial strain for different angles. When the rock mass is damaged, the distribution of velocity and seepage pressure in the rock mass varies significantly under the influence of different failure modes. While, when the precast fracture angle is 90°, the gas flows from the precast fracture to both sides along the shear rupture plane, forming a high-pressure zone along the rupture plane in the

Fig. 16 Damage amount evolution of fractured rock mass

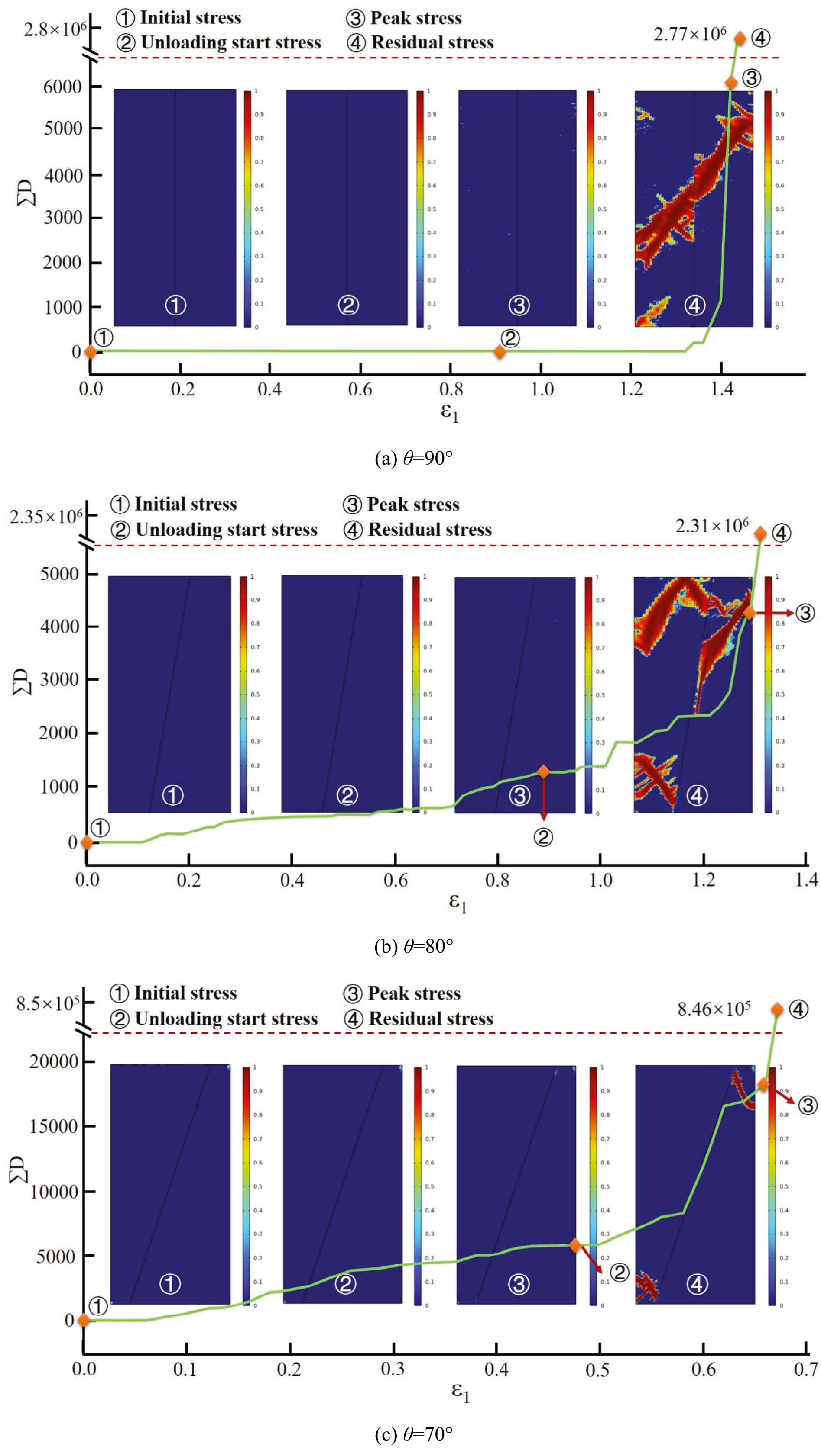

Fig. 17 Permeability evolution of fractured rock mass

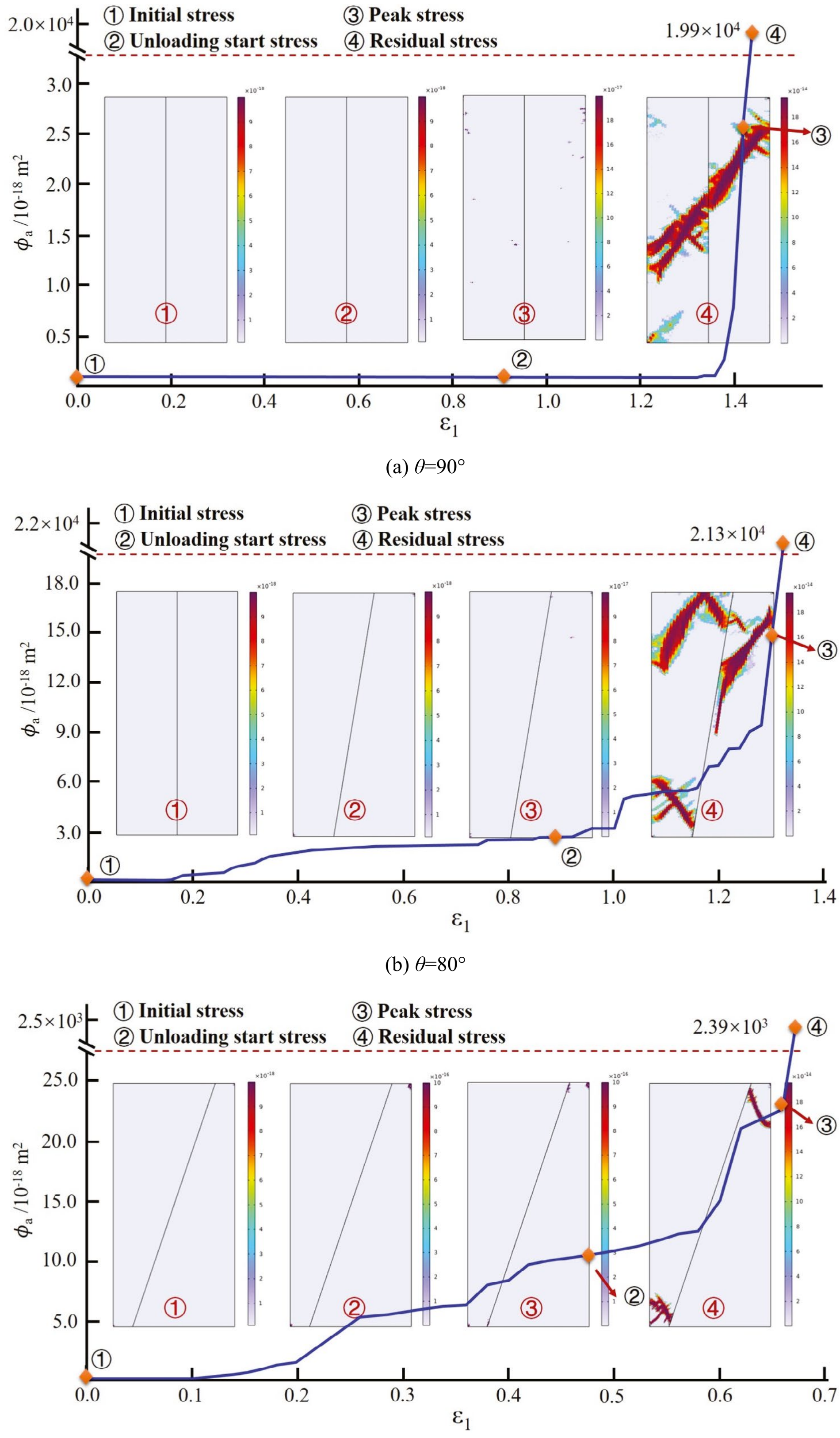

(a) θ=90°

(b) θ=80°

(c) θ=70°

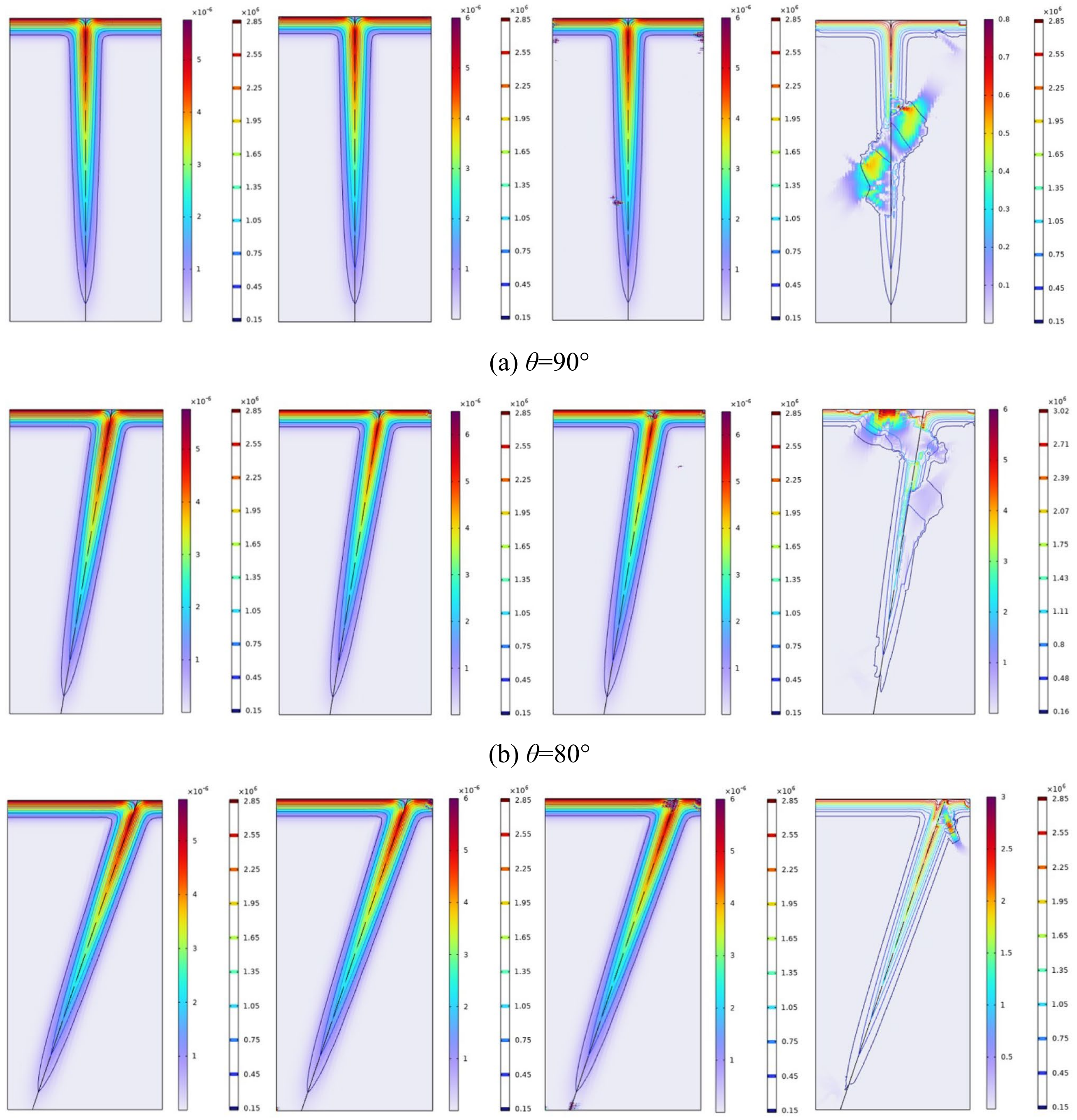

(a) θ=90°

(b) θ=80°

(c) θ=70°

Fig. 18 Seepage velocity and pressure evolution of fractured rock mass (the cloud map is the flow rate and the contour line is the pressure)

rock mass, while the pressure distribution and flow velocity at the rock mass seepage outlet has a little change. When the precast fracture angles are 80° and 70°, the seepage pressure are increased due to the expansion of the flow channel by the rupture plane on the inlet end of the rock mass. Therefore, the flow velocity inside the newly formed fractures increases significantly. On the outlet end, although the shear rupture plane intersects with precast fractures, the seepage pressure and the flow velocity within the precast fractures at the outlet end are relatively small. Therefore, the expansion of the fractures does not have a significant impact on the fluid flow rate in the rock mass. The rock failure mode and the relationship between the rupture plane and precast fractures significantly influence fluid flow in the rock mass. The generation of the

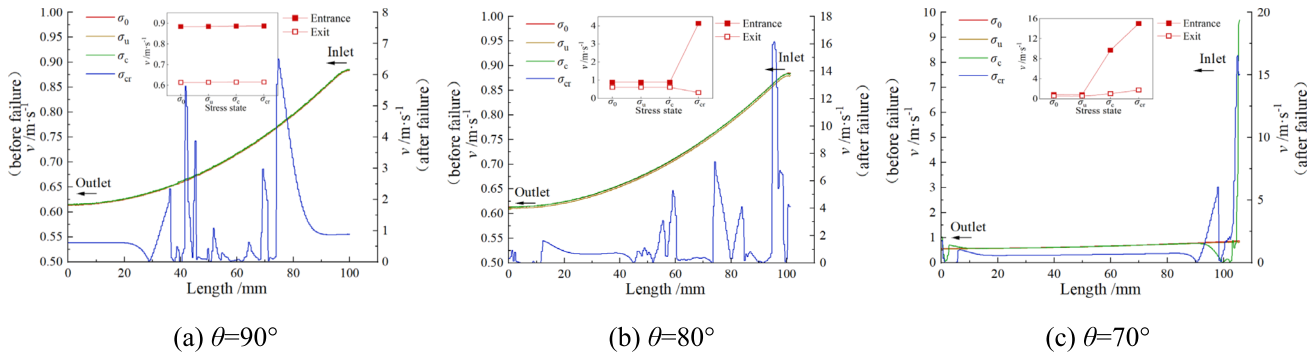

Fig. 19 Variation curve of flow velocity within fracture

rupture plane at the inlet end facilitates the increase in gas transport speed and flow rate. However, the increase in the rupture plane at the outlet end has a relatively small impact on fluid flow in the rock mass.

To do further analysis of the changes in the gas flow state within precast fractures during the loading and unloading processes, the variation curves of the flow velocity along the flow path of fractures under different stress states are plotted in Fig. 19. Based on the previous analysis, it is known that under the conditions of this study, the fluid within the fractures is in a linear laminar flow state, and the viscous resistance has a significant effect during the flow. Therefore, the gas flow velocity within the fractures rapidly decreases with the increase of the flow path, and with the increase in the stress levels, the difference in velocity between the inlet and outlet ends tends to increase. The analysis of the fracture flow velocity throughout the entire process of rock compression reveals that, before rock failure, there is a small difference in the flow velocity within the fractures, and the alteration in the velocity is positively correlated with the fracture aperture. After the failure of the rock mass, the flow velocities within the fractures all experience a significant increase. Particularly, when the fluid passes through the region influenced by the rupture plane, the velocity undergoes a sharp increase. However, the enhancement effect in the velocity diminishes with increasing the distance between the rupture plane and the inlet end of the rock mass. Moreover, the velocity rapidly decreases upon reaching the outlet end.

5.4 Damage-Seepage Characteristics of Rock Mass After Failure

The permeability characteristics of the rock mass under residual stress state are closely related to rock deformation and damage. Figure 20 shows the distribution of rock mass damage after the failure. Due to the relatively high confining pressure in the experimental conditions, the damage amount changes insignificantly with the increase in confining pressure. However, the damage amount shows a consistent decrease with the decrease of precast fracture angles under different confining pressures. Figure 21 illustrates the displacement of the rock mass after failure, while Fig. 22 depicts the distribution of seepage velocity and pressure in rock mass after failure. The deformation of the rock mass after failure significantly affects the precast fracture permeability. When the precast fracture angle is 90°, after failure, the upper and lower parts of the rock mass on the rupture plane undergo dislocation, resulting in obstruction to the flow of gas within the precast fractures. Additionally, after passing through the rupture plane, the gas inside the precast fractures diverts to both sides of the plane, lowering the precast fracture's permeability even more. Therefore, in comparison with the peak stress state, the increment in permeability after rock mass failure is relatively low. When the precast fracture angles are 80° and 70°, the end of the rock mass undergoes sliding after failure, leading to an increase in gas inlet. Although the diversion effect of the newly formed fractures to some extent reduces the gas flow within the precast fractures, the precast fractures do not undergo dislocation. Therefore, the permeability of the rock mass after failure is still significantly enhanced.

6 Conclusion

To deeply understand the deformation, failure mechanisms and seepage evolution characteristics of the fractured rock mass in gas-rich reservoir under loading and unloading conditions, a series of triaxial tests were conducted on rock masses under different confining pressures and precast fracture angles. Based on the elastic damage theory, the seepage theory of porous, fracture media, and the effective stress principle, a computational model for the coupling of fluid–solid-damage in fractured rock masses was established considering the influence of lateral stress on the fracture. Specific conclusions are as follows:

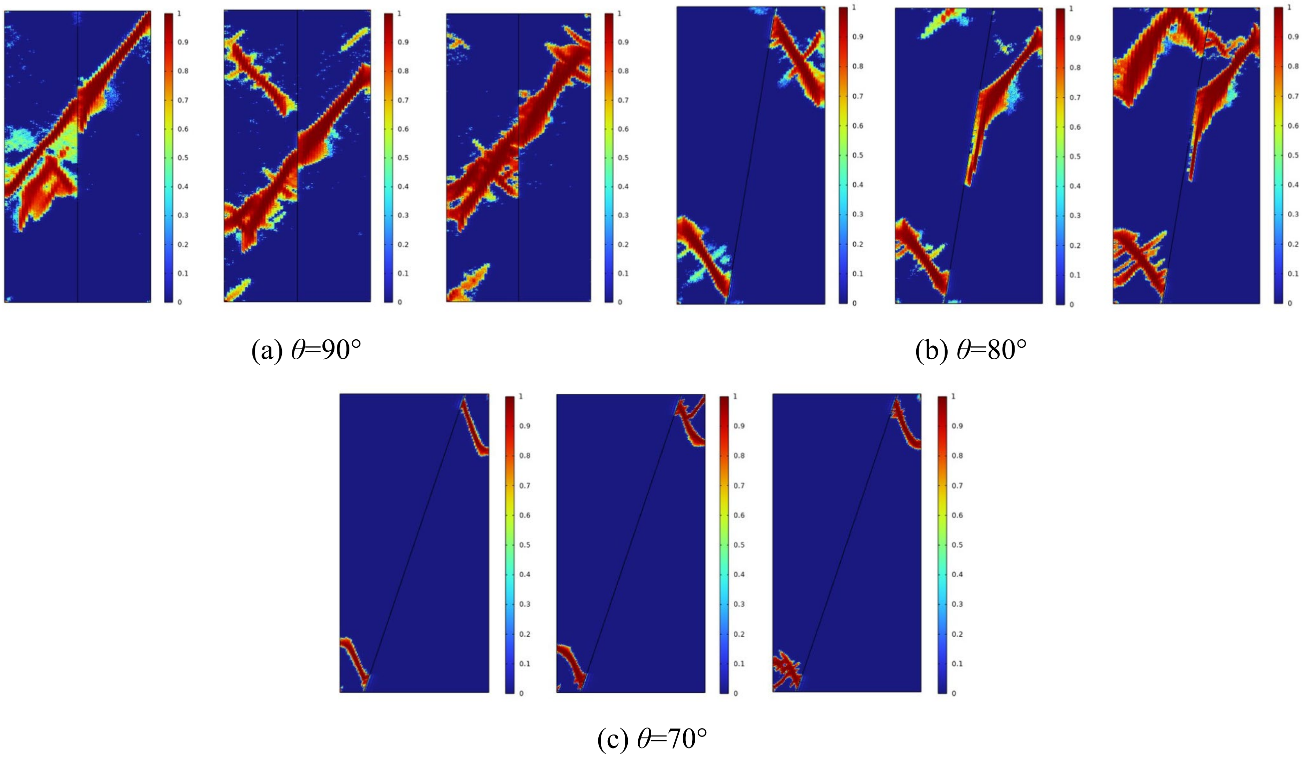

Fig. 20 Distribution of rock mass damage after failure

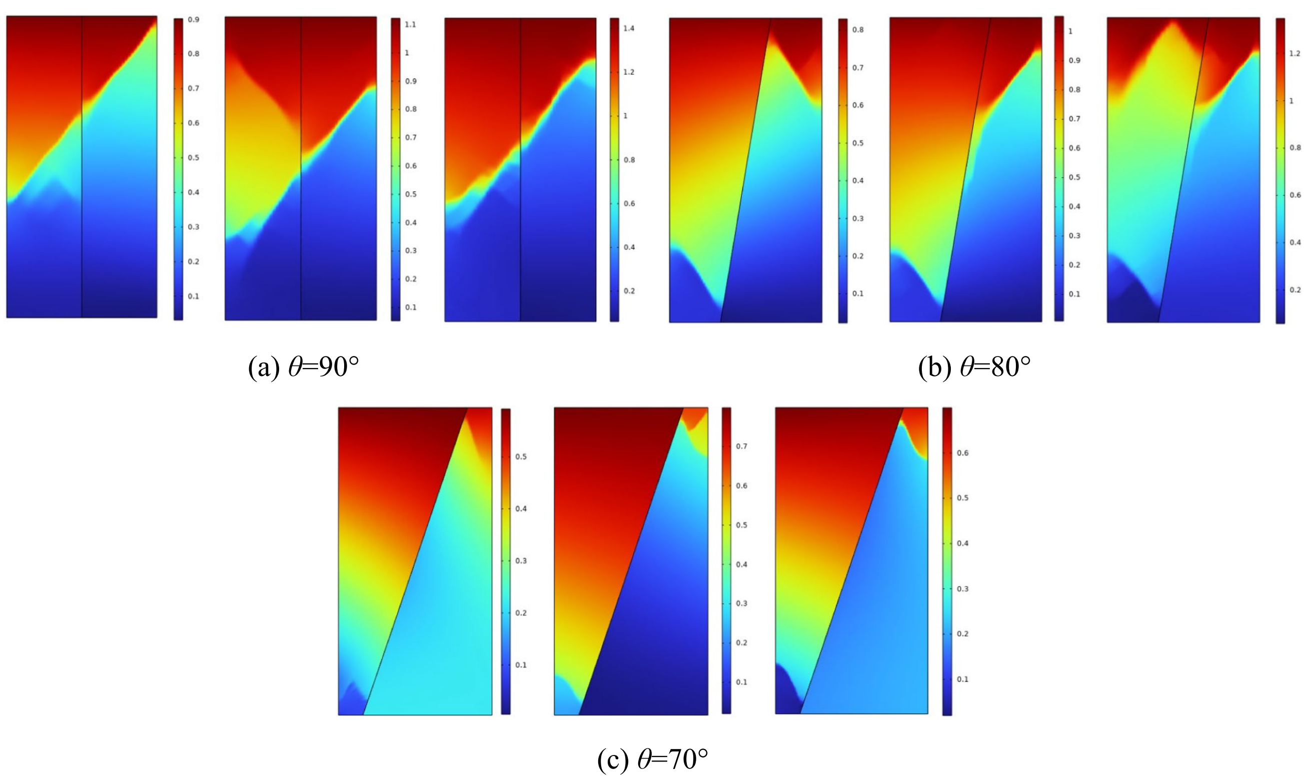

Fig. 21 Displacement of the rock mass after failure

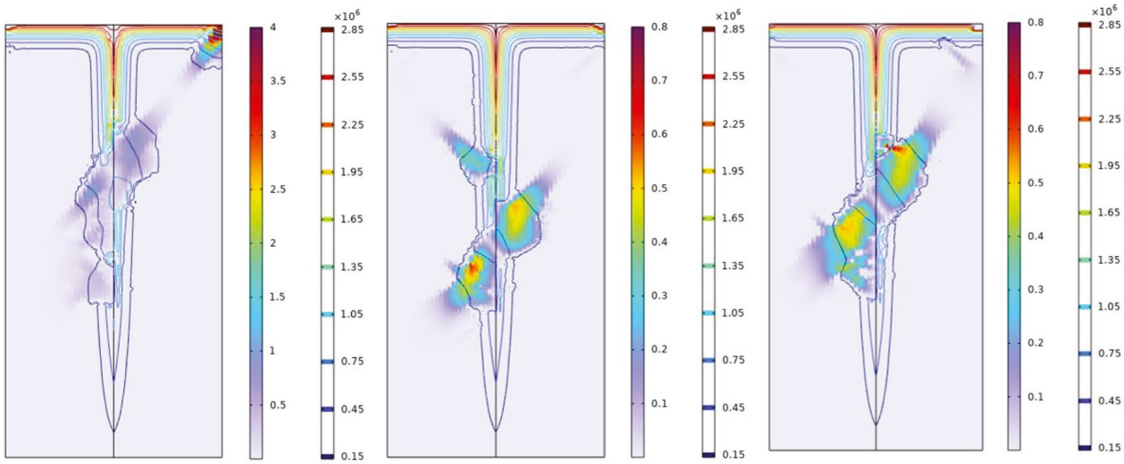

(a) θ=90°

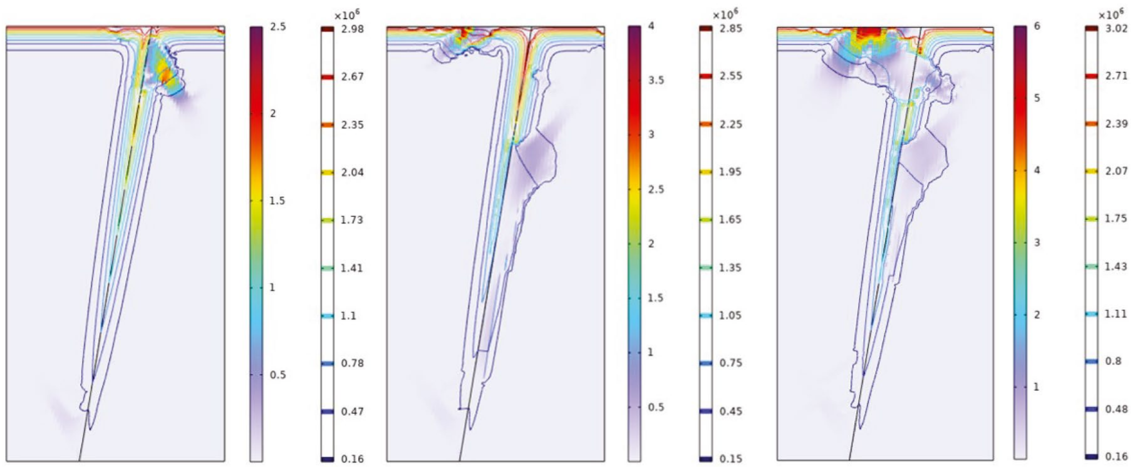

(b) θ=80°

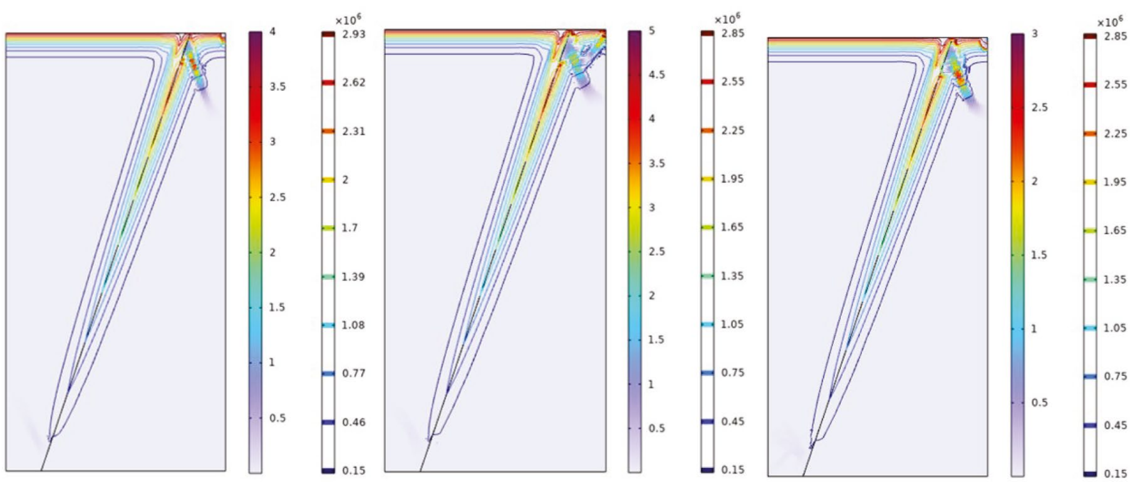

(c) θ=70°

Fig. 22 Distribution of seepage velocity and pressure in rock mass after failure (the cloud map is the flow rate and the contour line is the pressure)

(1) The development model of fracture volumetric strain changes from compression-unchanged-expansion to monotonic compression as the confining pressure increases and the fracture angle decreases. During the unloading stage, the fracture volumetric expansion phenomenon is the most pronounced feature, and the influence of the fracture angle on the rock mass fracture expansion is greater than that of the confining pressure.
(2) When the fracture angle is 90°, the failure type of the rock mass is a material failure, whereas, for fracture angles of 80° and 70°, the failure type of the rock mass is structural failure. Based on the deformation characteristics, the structural failure modes of the rock mass are classified into localized failure mode I and localized failure mode II. When the fracture angle is not less than 80° and the confining pressure is not less than 25 MPa, the failure mode is classified as localized failure mode II; otherwise, it is localized failure mode I.
(3) The effect of the lateral stress on the fracture surface increases the permeability of the rock mass. In addition, the permeability decreases with increasing the confining pressure and decreasing the fracture angle. At the same stress level, during the loading stage, the permeability of the rock mass linearly decreases with increasing the confining pressure. While, during the unloading stage, the permeability of the rock mass decreases nonlinearly with increasing the confining pressure, showing a rapid decrease followed by a slower decrease. Additionally, the larger the fracture angle, the more pronounced the nonlinearity.
(4) The numerical simulation results exhibit a high degree of agreement with experimental data. The established computational model for the coupling of fluid–solid-damage in fractured rock masses effectively captures the damage and failure mechanisms, as well as the evolution of seepage, during the loading and unloading processes. The change in the lateral stress influential coefficient on normal deformation χ with increasing the confining pressure exhibits logarithmic characteristics. Furthermore, the effect of the fracture angle on χ is significantly greater than that of the confining pressure. As the fracture angle decreases, the respective variation ranges of χ are: 0.005~0.03, 016~0.17, 0.2~0.22.
(5) During the loading and unloading phases, the damage amount increases with the decrease of precast fracture angle. However, after the failure of the rock mass, the damage amount decreases with the decrease of precast fracture angle. The variation in the permeability of the rock mass before the failure is primarily influenced by the deformation of the precast fractures. After the failure, the permeability of the rock mass is significantly influenced by the mode of failure.

Acknowledgements This work is supported by the National Natural Science Foundation for Young Scientists of China (Grant No. 52104076), the Graduate Research and Innovation Foundation of Chongqing, China (Grant No. CYB22032), the National Natural Science Foundation of China (Grant No. 52374079), the Science Foundation of State Key Laboratory of Coal Mine Disaster Dynamics and Control (China) (Grant No. 2011DA105287-MS202120). In addition, thanks to Dr. Lojain Suliman for checking the grammar and spelling of the manuscript.

Funding This study was funded by the National Natural Science Foundation of China (Grant No. 52104076 and 52374079), the Science Foundation of State Key Laboratory of Coal Mine Disaster Dynamics and Control (China) (Grant No. 2011DA105287-MS202120) and the China Postdoctoral Science Foundation (Grant No. 2023M730432).

Data availability Data associated with this research are available and can be obtained by contacting the corresponding author.

Declaration

Conflict of interest The authors declare that there are no conflicts of interest regarding the publication of this article.

References

Al-Bakri A, Sazid M (2023) (2023) Reconnaissance Geophysical Study on the Southeastern Part of Al-Qashah Aera, KSA. World J Eng Technol 11(3):424–433
Ansari TA, Singh HK, Sazid M, Singh HO, Singh TN, Singh KH, Zhou H (2020) Evaluation of various modes of fracture toughness (Mode I, II, and I + II) in Indian limestone based on AE parameters. Selected Studies in Geotechnics, Geo-informatics and Remote Sensing (CAJG 2020), pp 169–173
Ding YL, Yue ZQ (2022) Outburst characteristics of CO_2 gas-coal mixture with tunnel outburst simulator in deep mining. Geomech Geophys Geo-Energ Geo-Resour 8(1)
Du YT, Li TC, Li WT, Ren YD, Wang G, He P (2020) Experimental study of mechanical and permeability behaviors during the failure of sandstone containing two preexisting fissures under triaxial compression. Rock Mech Rock Eng 53(8):3673–3697
Gu LJ, Feng XT, Kong R, Yang CX, Han Q, Xia YL (2023) Excavation stress path induced fracturing mechanism of hard rock in deep tunnel. Rock Mech Rock Eng 56(3):1779–1806
Gong YF, Zhai S, Zha YQ, Xu TH, Liu S, Kang B, Zhang BL (2022) Numerical simulation of embedded discrete-fracture seepage in deep carbonate gas reservoir. Energies 15(19):7237
Hamiel Y, Liu YF, Lyakhovsky V, Ben-Zion Y, Lockner D (2004) A viscoelastic damage model with applications to stable and unstable fracturing. Geophys J Int 159(3):1155–1165
Huo ZG, Xue WT, Shu LY (2021) Exploration on outburst mechanism of rock and carbon dioxide in coal mines of China. Coal Sci Technol 49(1):155–161 ((**in Chinese**))
Katsuki D, Gutierrez M, Almrabat A (2019) Stress-dependent shear wave splitting and permeability in fractured porous rock. J Rock Mech Geotech Eng 11(1):1–11
Lee SH, Lee KK, Yeo IW (2014) Assessment of the validity of Stokes and Reynolds equations for fluid flow through a rough-walled fracture with flow imaging. Geophys Res Lett 41(13):4578–4585
Lei QH, Doonechaly NG, Tsang CF (2021) Modelling fluid injection-induced fracture activation, damage growth, seismicity

occurrence and connectivity change in naturally fractured rocks. Int J Rock Mech Min Sci 138:104598
Li H, Zhong RZ, Pel L, Smeulders D, You ZJ (2023) A new volumetric strain-based method for determining the crack initiation threshold of rocks under compression. Rock Mech Rock Eng 57:1329–1351
Li M, Liu XS (2021) Experimental and numerical investigation of the failure mechanism and permeability evolution of sandstone based on hydro-mechanical coupling. J Nat Gas Sci Eng 95:104240
Liu CH, Chen CX (2007) Seepage characteristics of rock single fracture under three-dimensional stress. Adv Nat Sci 17(7):989–994 ((**in Chinese**))
Liu SM, Wang DK, Yin GZ, Li MH, Li XL (2020) Experimental study on the microstructure evolution laws in coal seam affected by temperature impact. Rock Mech Rock Eng 53(3):1359–1374
Liu QL, Wang EY, Kong XG, Li Q, Hu SB, Li DX (2018a) Numerical simulation on the coupling law of stress and gas pressure in the uncovering tectonic coal by cross-cut. Int J Rock Mech Min Sci 103:33–42
Liu XR, Kou MM, Lu YM, Liu YQ (2018b) An experimental investigation on the shear mechanism of fatigue damage in rock joints under pre-peak cyclic loading condition. Int J Fatigue 106:175–184
Ma D, Miao XX, Chen ZQ, Mao XB (2013) Experimental investigation of seepage properties of fractured rocks under different confining pressures. Rock Mech Rock Eng 46(5):1135–1144
Ma HC, Wang JP, Feng PC, Qian JZ, Tan XH, Luo QK (2022) Effect of high confining pressure on flow behavior and hydraulic aperture considering fractured rock deformation. Geomech Geophys Geo-Energ Geo-Resour 8(5)
Ma HC, Feng PC, Qian JZ, Deng YP, Wu DX (2023a) Study on the seepage mechanisms of rock with bifurcation fractures under confining pressure. Hydrogeol J 31(7):1701–1713
Ma TR, Jiang LT, Shen WJ, Cao WZ, Guo CB, Nick HM (2023b) Fully coupled hydro-mechanical modeling of two-phase flow in deformable fractured porous media with discontinuous and continuous Galerkin method. Comput Geotech 164:105823
Ma LQ, Khan MN, Feroze T, Sazid M, Cao KW, Hussain S, Gao QQ, Alarifi SS, Wang H (2024) Prediction of rock loading stages using average infrared radiation temperature under shear and uniaxial loading. Infrared Phys Technol 36:105084
Mukai A, Yamauchi T, Ishii H, Matsumoto S (2007) In situ stress measurement by the stress relief technique using a multi-component borehole instrument. Earth Planets Space 59(3):133–139
Sazid M, Hussein K, Abudurman K (2023) Rock stress measurement methods in rock mechanics—a brief overview. World J Eng Technol 11(2):252–272
Singh AB (1997) Study of rock fracture by permeability method. J Geotech Geoenviron Eng 123(7):601–608
Song ZX, Zhang JW, Wu SK (2023) Energy dissipation and fracture mechanism of layered sandstones under coupled hydro-mechanical unloading. Processes 11(7):2041
Vu MN, Nguyen ST, To QD, Dao NH (2017) Theoretical predicting of permeability evolution in damaged rock under compressive stress. Geophys J Int 209(2):1352–1361
Walsh R, McDermott C, Kolditz O (2008) Numerical modeling of stress-permeability coupling in rough fractures. Hydrogeol J 16(4):613–627
Wang HL, Xu WY, Zuo J (2014) Compact rock material gas permeability properties. Phys B Condens Matter 449:10–18
Wang JP, Ma HC, Qian JZ, Feng PC, Tan XH, Ma L (2021) Experimental and theoretical study on the seepage mechanism characteristics coupling with confining pressure. Eng Geol 291:106224
Wang PF, Xie YS (2022) Numerical simulation of fracture failure characteristics of rock-mass with multiple nonparallel fractures under seepage stress coupling. Geotech Geol Eng 40(5):2769–2779
Wang ZH, Ren WG, Tan YL, Konietzky H (2020) Experimental and numerical study on hydromechanical coupled deformation behavior of beishan granite considering permeability evolution. Geofluids 2020:1–14
Watanabe N, Hirano N, Tsuchiya N (2008) Determination of aperture structure and fluid flow in a rock fracture by high-resolution numerical modeling on the basis of a flow-through experiment under confining pressure. Water Resour Res 44(6)
Yan BQ, Qi QJ, Liu JZ, Cai MF, Li XS, Wang PT (2022) Fracture propagation and permeability evolution mechanism of jointed rock mass in coastal mines. Rock Mech Rock Eng 56:2763–2778
Yang SQ, Hu B (2020) Creep and permeability evolution behavior of red sandstone containing a single fissure under a confining pressure of 30 MPa. Sci Rep 10(1)
Yang W, Wang H, Lin BQ, Wang YK, Mao XBA, Zhang JG, Lyu YC, Wang M (2018) Outburst mechanism of tunnelling through coal seams and the safety strategy by using "strong-weak" coupling circle-layers. Tunn Undergr Space Technol 74:107–118
Yuan CL, Xian XH, Chai XQ (2022) Study on comprehensive disaster control mode of coal and gas (CO_2) outburst and steep coal steam. China Coal 48(S2):180–186 ((**in Chinese**))
Zhang D, Zhang LM, Wang ZQ, Meng FZ, Wen JH, Gao LY (2024) Multi-level loading of the seepage pressure in filled cracked sandstone: Seepage-creep mechanical characteristics and crack initiation mechanism. Eng Fract Mech 300:109991
Zhang K, Zheng WB, Xu C, Chen SG (2019) Risk assessment of gas outburst in tunnels in non-coal formation based on the attribute mathematical theory. Geomat Nat Haz Risk 10(1):483–504
Zhang Y, Zhang J, Du W, Wang H, Niu K (2021) Gas seepage under continuous and step loading based on true triaxial seepage test apparatus. Exp Tech 45(2):121–132
Zhang HM, Yuan C, Chen SG, Yang GS, Xia HJ (2022a) Experimental study of fracture geometry characteristics on rock mass strength and crack propagation evolution law. Eur J Environ Civ Eng 26(16):7972–8001
Zhang YB, Liu XR, Guo PS, Jia P, Yang TH, Ren FY (2022b) Quantifying strength and permeability of fractured rock mass using 3D bonded block numerical model. J Petroleum Sci Eng 208:109592